

JGR Planets

RESEARCH ARTICLE

10.1029/2020JE006589

Key Points:

- The Th distribution in the South Pole-Aitken Basin is consistent with mantle-derived ejecta influenced by subsequent geologic events
- Th-bearing materials exhibit a Ti-bearing gabbroan composition consistent with globally distributed late lunar magma ocean cumulates
- South Pole-Aitken impact melt is low-Ca pyroxene-rich and low-Th, suggesting stratification in the upper mantle at the time of formation

Supporting Information:

- Supporting Information S1

Correspondence to:

D. P. Moriarty III,
daniel.p.moriarty@nasa.gov







Citation:

Moriarty, D. P., Watkins, R. N., Valencia, S. N., Kendall, J. D., Evans, A. J., Dygert, N., & Petro, N. E. (2021). Evidence for a stratified upper mantle preserved within the south pole-Aitken Basin. *Journal of Geophysical Research: Planets*, 121, e2020JE006589. <https://doi.org/10.1029/2020JE006589>

Received 18 JUN 2020

Accepted 8 DEC 2020

Evidence for a Stratified Upper Mantle Preserved Within the South Pole-Aitken Basin

D. P. Moriarty III^{1,2} , R. N. Watkins³ , S. N. Valencia^{1,2} , J. D. Kendall^{1,4}, A. J. Evans⁵ , N. Dygert⁶ , and N. E. Petro¹ 

¹NASA Goddard Space Flight Center, Greenbelt, MD, USA, ²University of Maryland, College Park, MD, USA, ³Planetary Science Institute, Tucson, AZ, USA, ⁴University of Maryland Baltimore County, Baltimore, MD, USA, ⁵Brown University, Providence, RI, USA, ⁶University of Tennessee, Knoxville, TN, USA

Abstract The evolution and compositional structure of the lunar mantle has been extensively modeled but insufficiently constrained by observations. Here, we identify and characterize mantle materials exposed by the Moon's largest impact basin to better understand the composition, stratigraphy, and evolution of the upper mantle. The vast South Pole-Aitken Basin (SPA) exhibits a broad, crescent-shaped thorium and potassium distribution. These incompatible elements are predicted to be concentrated in the dregs of the lunar magma ocean during end-stage crystallization. Through consideration of basin formation models convolved with subsequent geologic evolution, we demonstrate that the distribution and implied stratigraphy of Th- and K-bearing materials across SPA are consistent with an upper mantle ejecta origin. The most pristine exposures of these materials are confined to northwest SPA and also exhibit elevated Ti and Fe (relative to the farside highlands) in association with a gabbroan mineralogy. This is consistent with late-stage magma ocean assemblages predicted by petrologic models. In contrast, SPA impact melt derived from greater depths is associated with a low-Ca pyroxene-dominated assemblage. Together, these compositional patterns are evidence for a stratified ancient upper mantle. Importantly, the incompatible-element-enriched, ilmenite-bearing ferroan gabbroan cumulates evidently had not participated in gravitational overturn at the time of SPA formation. Contrary to recent hypotheses invoking nearside sequestration of incompatible elements to explain hemispherical differences in crustal building and volcanic resurfacing, it follows that incompatible elements were globally distributed in the magma ocean at the time of SPA formation.

Plain Language Summary Like the Earth, the Moon is layered into a crust and mantle. The Moon's layering was shaped by an early global melting event known as the "Lunar Magma Ocean." As the magma ocean solidified, dense minerals sank to form the mantle, while less-dense minerals floated to form the crust. Elements such as thorium are not easily incorporated into mineral structures, and remain in the liquid. Because of this, a thorium-rich dreg layer was sandwiched between the crust and mantle. These dregs are very dense and are expected to sink into the underlying mantle during or soon after crystallization.

We demonstrate that the Moon's largest and oldest impact basin excavated material from this dense, thorium-rich layer before it sank. The exposed material was then diluted and obscured by four billion years of impact cratering and volcanic eruptions. However, we identify several pristine exposures created by recent craters.

The impact basin also melted rocks from greater depths than the rocks it ejected. These melted rocks exhibit a much different composition. This indicates that the lunar upper mantle included two compositionally distinct layers that were exposed in different ways by this large impact event. These results have important implications for understanding the formation and evolution of the Moon.

1. Introduction

Through human exploration, robotic landers, telescopic observations, orbital data, and sample analyses, lunar scientists have developed a rich understanding of the Moon. However, a number of important science questions remain unanswered. One of the highest-priority science goals is to understand the composition, formation, and subsequent evolution of the lunar crust and mantle (e.g., National Research Council, 2007).

Although several lunar impact basins are expected to excavate material from near or below the crust-mantle boundary (e.g., Melosh et al., 2017; Miljkovic et al., 2015), mantle materials have not yet been unambiguously identified, either on the lunar surface through remote sensing observations or in analyses of returned samples (e.g., Tartèse et al., 2019). This ambiguity is due in part to a lack of agreement among researchers regarding the compositional stratigraphy of the upper mantle.

As there are no confirmed primary mantle materials in the lunar sample collection (Shearer et al., 2015), our understanding of the mantle is derived primarily from laboratory experiments, geophysical observations, and petrological analyses of crustal materials, volcanic glasses, and mare basalts. Although these investigations provide valuable insight, a number of fundamental issues remain unresolved detailing the formation and evolution of the mantle from solidification of a Lunar Magma Ocean (LMO) (e.g., Boukare et al., 2018; Dygert et al., 2016; Elardo et al., 2011; Elkins-Tanton et al., 2011, 2017; Lin et al., 2017; Zhao et al., 2019). The magma ocean's depth, bulk composition, crystallization sequence, dynamical evolution, and thermal evolution all affect the structure and properties of the Moon's juvenile mantle, influencing its petrologic evolution. As we enter into a new era of lunar exploration, identifying and characterizing mantle materials exposed on the lunar surface is critically important to gaining insights into the evolution of the mantle and the LMO processes that preceded it (Tartèse et al., 2019). Here, we investigate the possibility that distinctive thorium-bearing materials in the Moon's largest impact basin represent excavated mantle materials currently exposed on the lunar surface.

2. Background

2.1. Formation of the Lunar Crust and Mantle from a Magma Ocean

The early Moon is thought to have formed from a giant impact with the Earth, and its current crust and mantle are products of a global magma ocean. Estimates of the magma ocean's depth range from several hundred km to the entire Moon (e.g., Steenstra et al., 2020; Wood et al., 1970). As the LMO cooled, minerals fractionally crystallized in a specific sequence depending on melt composition, pressure, oxygen fugacity, and temperature. Magnesian olivine was the first mineral to crystallize, followed by an orthopyroxene-bearing assemblage gradually transitioning from magnesian to more ferroan (Buck & Toksöz, 1980; Charlier et al., 2018; Elardo et al., 2011; Elkins-Tanton et al., 2011; Hess and Parmentier, 1995; Lin et al., 2017; Rapp & Draper, 2018; Snyder et al., 1992; van Orman & Grove, 2000). Because olivine and orthopyroxene are denser than the coexisting liquid, these minerals sank, forming a cumulate stratigraphy related to the crystallization sequence. After ~70%–80% crystallization, anorthite minerals began to crystallize (Buck & Toksöz, 1980; Charlier et al., 2018; Elkins-Tanton et al., 2011; Hess & Parmentier, 1995; Lin et al., 2017; Rapp & Draper, 2018; Snyder et al., 1992). Anorthite is less dense than the coexisting liquid, and floated to form the anorthositic crust. Meanwhile, the co-crystallizing mafic cumulates (at this stage including low-Ca pyroxenes (orthopyroxene and/or pigeonite) as well as high-Ca clinopyroxenes) sank. The final minerals to crystallize from the residual liquid (LMO dregs) are highly ferroan and are thought to include some combination of low-Ca pyroxene, clinopyroxene, olivine, anorthite, and oxides such as ilmenite (Charlier et al., 2018; Lin et al., 2017; Rapp & Draper, 2018; Snyder et al., 1992).

Although the precise mineral compositions and proportions forming from the LMO dregs are model dependent, a reasonable approximation was described by Elkins-Tanton et al. (2011) as 30% low-Ca pyroxene, 20% high-Ca pyroxene, 40% anorthite, and 10% oxides. In general, the final assemblage is ferroan and roughly gabbronoritic, i.e., composed of roughly similar proportions of low-Ca pyroxenes and high-Ca pyroxenes (constituting between 40% and 90% of the bulk rock) with 10%–60% plagioclase. This definition for lunar gabbronorites was established by Tompkins and Pieters (1999) in a lunar rock classification scheme modified from that of Stoffler et al. (1980). Depending on the efficiency of plagioclase flotation, anorthite

may have continued to float even at this late stage (Dygert et al., 2017), which would have result in a lower anorthite content in the LMO dreg assemblage.

The LMO dregs are also associated with a distinctive incompatible element signature. During LMO crystallization, certain elements did not readily substitute into early forming minerals (i.e., olivine and orthopyroxene). Because of this, the residual magma ocean liquid became increasingly enriched in these incompatible elements as solidification progressed (e.g., Warren & Wasson, 1979). These incompatible elements include titanium, thorium, and “KREEP”: potassium (**K**), rare earth elements, and phosphorus (**P**) (Warren & Wasson, 1979). As the last assemblage to crystallize, the ferroan, gabbro-noritic LMO dreg assemblage was highly enriched in these incompatible elements.

The ferroan, gabbro-noritic, incompatible-rich LMO dreg layer is often referred to as “urKREEP” (Warren & Wasson, 1978), but there is some disagreement within the lunar science community as to whether this refers specifically to the liquid dregs or the resulting crystallized assemblage. Here, we treat this term as convenient shorthand for either product. Although the urKREEP dregs are initially sandwiched between the plagioclase flotation crust and the underlying ultramafic mantle cumulates by the end of LMO solidification, they may not have persisted in that stratigraphy.

2.2. Gravitational Restructuring via Cumulate Mantle Overturn

Because crystallizing minerals are progressively enriched in dense elements (KREEP, Fe, Ti) as LMO crystallization proceeds, the initial mantle cumulate stratigraphy is gravitationally unstable (e.g., Hess & Parmentier, 1995; Ringwood & Kesson, 1976). For this reason, it is thought that the lunar mantle underwent gravitationally driven restructuring, where magma ocean cumulates were redistributed according to their densities. This process is known as cumulate mantle overturn.

The exact nature of this restructuring is not currently known. Models of the timing, nature, and scale of this restructuring suggest endmember outcomes ranging from large-scale solid-state cumulate overturn (Elkins-Tanton et al., 2011; Hess & Parmentier, 1995) to a multistage process involving homogenization of basal mafic cumulates through basal overturn (Boukare et al., 2018) followed by localized downwelling of ilmenite-bearing cumulate diapirs contemporaneous with LMO solidification (C. Li et al., 2019; Perret-Fisher et al., 2019; Zhao et al., 2019).

As urKREEP hosts the densest products of LMO crystallization, it is a critical component of cumulate overturn. If the urKREEP dregs crystallized in bulk and remained in situ, this would produce an urKREEP layer 10s of km thick in the uppermost mantle (e.g., Elkins-Tanton et al., 2011). However, this may be an unlikely outcome according to recent models and experiments exploring mantle dynamics. Dense urKREEP products are thought to overturn on timescales of 10s of millions of years or less (C. Li et al., 2019; Yu et al., 2019; Zhao et al., 2019). This is significantly shorter than the 100-Myr timescale of LMO crystallization (Borg et al., 2019, 2011; Elkins-Tanton et al., 2011; Maurice et al., 2020; Thiemens et al., 2019). This suggests that urKREEP dregs may have begun downwelling before LMO crystallization was complete, in some scenarios mixing with the underlying ultramafic cumulates to form a thickened incompatible-element-bearing layer in the upper mantle before ultimately sinking into the lower mantle (Dygert et al., 2016; Hess & Parmentier, 1995; C. Li et al., 2019).

Regardless of the specific conditions under which it proceeded, mantle overturn is thought to play a critical role in the thermal and geophysical evolution of the Moon. Mantle overturn may have contributed to the onset of mare volcanism by influencing mantle convection, concentrating heat-producing radioactive elements in the lower mantle, and depressing the melting point (e.g., Elardo et al., 2020; Hess & Parmentier, 1995). In addition to mare basalt production, heat-producing elements delivered near the core-mantle boundary may have also contributed to the partial melt layer in the lower mantle implied by viscous dissipation and seismic observations (e.g., Harada et al., 2014; Khan et al., 2014; Weber et al., 2011; N. Zhang et al., 2017).

In addition to producing a vertical distribution of incompatible elements in the lunar mantle, cumulate mantle overturn may have also influenced the lateral distribution. The lunar surface exhibits hemispherical

differences in crustal thickness, volcanic resurfacing rates, and geochemistry that have been previously attributed to sequestration of KREEP on the lunar nearside through various processes (Arai et al., 2008; Cadogan, 1974; Gross & Joy, 2016; Loper & Werner, 2002; Wasson & Warren, 1980; Whitaker, 1981). This hemispherical asymmetry in KREEP distribution may have arisen from cumulate overturn via long-wavelength gravitational instabilities (e.g., Parmentier et al., 2002). In this case, KREEP would have been initially globally distributed in the magma ocean dregs, and sequestered on the nearside through large-scale (hemispheric) downwelling. Alternatively, KREEP may have been preferentially concentrated on the nearside during LMO crystallization through asymmetric crystallization processes (e.g., Loper & Werner, 2002; Wasson & Warren, 1980). In this case, the lunar farside would not exhibit a notable KREEP enhancement.

2.3. Resulting Lunar Structure and the Search for Mantle Exposures

Based on Gravity Recovery and Interior Laboratory (GRAIL) gravity measurements, LMO crystallization formed a low-density ($\sim 2,550 \text{ kg/m}^3$) plagioclase-dominated crust up to $\sim 43 \text{ km}$ thick (Wieczorek et al., 2013). Although the crust is dominated by plagioclase, remote sensing and geophysical observations suggest the lower portion of the crust may host mafic minerals (Cahill et al., 2009; Roberts et al., 2019; Spudis & Davis, 1986; Spudis et al., 2014; Sun et al., 2017; Tompkins & Pieters, 1999; Wieczorek & Zuber, 2001b). Underlying mantle materials are significantly denser ($\sim 3,360 \text{ kg/m}^3$; Taylor & Wieczorek, 2014; Wieczorek et al., 2013), due to a paucity of plagioclase (Dyger et al., 2017) and the presence of mafic minerals and oxides (e.g., Elkins-Tanton et al., 2011).

Impact models and scaling laws suggest that large impact basins postdating LMO crystallization have excavated upper mantle material (e.g., Miljkovic et al., 2015) from beneath the anorthositic crust. Identifying and characterizing excavated mantle materials across the lunar surface is critical for understanding the formation and evolution of the Moon. These materials are promising targets for future missions and analyses.

A popular assumption that low-density magnesian olivine cumulates ascended from depth to replace sinking higher-density ferroan cumulates has led many researchers to focus on olivine as a tracer of lunar mantle exposures. However, analyses of remote sensing data and lunar samples do not support the existence of large-scale olivine-rich units in impact basins. Olivine does not dominate large basin structures where mantle materials may be exposed (Lemelin et al., 2019; Wieczorek & Phillips, 1998; Yamamoto et al., 2010). Where observed in remote sensing data, olivine often occurs in small, localized exposures typically embedded within anorthositic materials, suggesting a possible crustal origin (Prissel & Gross, 2020).

Instead, the largest basins on the Moon tend to exhibit low-Ca pyroxene-dominated lithologies in their impact melt and ejecta (Crites & Lucey, 2015; Hurwitz & Kring, 2014; Lemelin et al., 2019; Melosh et al., 2017; Moriarty et al., 2013; Moriarty & Pieters, 2018; Nakamura et al., 2009; Ohtake et al., 2014; Runyon et al., 2020). This, along with geophysical observations, has been invoked to argue that the upper mantle is dominated by pyroxenes (Hurwitz & Kring, 2014; Kuskov et al., 2015; Melosh et al., 2017).

Largely absent from this discussion are gabbroanorthitic, ferroan, KREEP-rich, ilmenite-bearing late-stage cumulates of the LMO (i.e., urKREEP). Were such materials excavated by basin-forming impacts before the presumed gravitational restructuring events occurred? Or, alternatively, if some fraction of the late LMO cumulates did not participate in this gravitational restructuring?

As the largest ($>2,000 \text{ km}$), deepest, and most ancient confirmed impact structure on the Moon, the South Pole-Aitken Basin (SPA) is an excellent candidate in the search for excavated lunar mantle. SPA is modeled to have excavated and melted large volumes of mantle materials (Hurwitz & Kring, 2014; Melosh et al., 2017; Potter et al., 2012; Uemoto et al., 2017; Vaughan & Head, 2014). The SPA interior exhibits distinctive geochemical properties (e.g., Jolliff et al., 2000), including broad iron and thorium anomalies and a pyroxene-dominated mineralogical signature (Borst et al., 2012; Hu et al., 2019; Huang et al., 2020; Lawrence et al., 2000; Lucey et al., 1998; Moriarty & Pieters, 2018; Ohtake et al., 2014; Pieters et al., 2001). Additionally, the basin exhibits unusual volcanic (Chen et al., 2020; Hagerty et al., 2011; Ivanov et al., 2018; Moriarty & Pieters, 2015, 2018; Pasckert et al., 2018; Pieters et al., 2001; Whitten & Head, 2015; Yingst and Head, 1999) and geophysical (James et al., 2019) properties. While SPA exhibits a lower degree of mare volcanism than nearside basins, features such as Mons Marguerite (formerly Mafic Mound) and the SPA Compositional

Anomaly (SPACA) appear to be volcanic resurfacing deposits with mineralogies distinct from typical mare basalts (Moriarty & Pieters, 2015, 2018), suggesting a unique and localized thermal and magmatic history.

Related to this unique thermal history is the role and fate of heat-producing incompatible elements on the lunar farside. Thorium, an important proxy for these incompatible elements, has been observed within SPA (e.g., Lawrence et al., 2002b). The origin of SPA's thorium-bearing material is still under debate. Historically, much of this debate has focused on two thorium "hotspots" within the northwest quadrant of the basin. Several origin scenarios have been proposed, including antipodal ejecta from nearside basins (Haskin et al., 1998; Lawrence et al., 2000; Stuart-Alexander, 1978; Wieczorek & Zuber, 2001a), lower crust (or upper mantle) exposed by SPA (Garrick-Bethell & Zuber, 2005; Lawrence et al., 2000), and postSPA Mg-suite igneous plutons in the lower crust (Hagerty et al., 2011; Haskin et al., 2004).

Here, we investigate the possibility that thorium-bearing materials within SPA are excavated from the mantle, specifically the ferroan, gabbro-noritic, ilmenite-bearing cumulates predicted to form in the final stages of LMO crystallization (i.e., urKREEP). Our primary analyses focus on integrating Lunar Prospector thorium abundance data with mineralogical assessments from Moon Mineralogy Mapper (M^3) data. These results are interpreted in the context of models of SPA formation and LMO crystallization.

3. Distribution and Evolution of Mantle-Derived SPA Ejecta

Were mantle materials excavated by the SPA-forming impact? If so, what was the resulting distribution across the lunar surface? Although these questions have not been definitively answered through observations, it is possible to understand likely ejecta behavior through impact models.

Building upon previous two-dimensional impact models (e.g., Potter et al., 2012), recent three-dimensional models (Melosh et al., 2017) confirm that abundant mantle materials should have been excavated during the SPA-forming impact (Figure 1). Assuming an average farside crustal thickness of 45 km (consistent with GRAIL data; Wieczorek et al., 2013), ejecta originating from depths of 45–105 km are interpreted to originate from the upper mantle, and are expected to be dominated by mafic minerals and oxides. Ejecta from depths shallower than 45 km are interpreted to originate from the feldspathic crust. According to Melosh et al. (2017), reasonable model parameters (200 km impactor diameter and a 45° impact angle) result in a crescent-like distribution of mantle-derived ejecta, thicker than 10 km in places (Figure 1). The distribution is centered downrange, and predicted to be thickest within the northwest quadrant of SPA (Figure 1). This impact angle is consistent with magnetic anomalies in NW SPA (Figure S1; Tsunakawa et al., 2010), which may result from downrange remnants of a Fe-rich impactor or mantle ejecta (Cahill et al., 2014; Wieczorek et al., 2012).

Of course, it is not expected that pure mantle materials are preserved on the lunar surface in this exact geometry. Starting with the impact event itself, SPA mantle ejecta were subject to roughly 4.3 billion years (Evans et al., 2018) of geologic processing resulting in dilution, obscuration, and redistribution. These processes include:

1. *Mixing with crustal SPA impact ejecta:* Within the thickest zone of the SPA ejecta deposit, the ratio between crust- and mantle-derived ejecta was approximately 1:1 (Melosh et al., 2017). Although local variations may persist, it is likely that the ejecta deposit was well-mixed to some degree due to the high-energy, kinetic nature of ejection and emplacement
2. *Mixing with target crust via ballistic sedimentation during SPA ejecta emplacement:* On airless bodies such as the Moon, ejecta emplacement occurs ballistically (e.g., Oberbeck, 1975). During this process, the ejecta mixes to some degree with the underlying crustal substrate (Petro and Pieters, 2008). In SPA, this process would have resulted in further dilution of mantle-derived ejecta
3. *Inward translation and mixing during basin modification:* As suggested by impact models and remote sensing observations, the thickest portion of the SPA ejecta deposit was emplaced exterior to the transient cavity, but interior to the final topographic rim of the basin (Garrick-Bethell & Zuber, 2009; Potter et al., 2012; Melosh et al., 2017) (Figure 1). Therefore, the ejecta deposit was significantly affected by the modification stage of basin formation. During collapse of the transient cavity, the ejecta deposit underwent translation toward the basin center (Potter et al., 2012). Because the modification stage involves

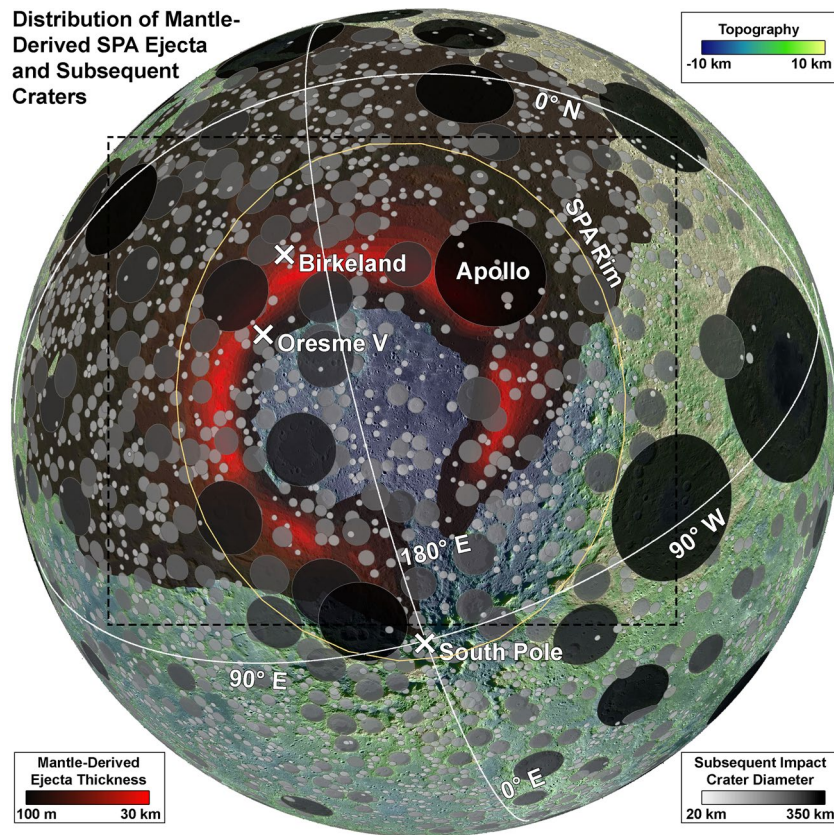


Figure 1. The distribution of mantle-derived ejecta emplaced by the SPA-forming impact estimated by three-dimensional impact models (Melosh et al., 2017). The ejecta blanket was subsequently modified by a number of processes, including impact cratering. Here, impact craters 20 km and larger are shown (Head et al., 2010; Kadish et al., 2011), although this catalog underrepresents craters <50 km in diameter by >10% (Robbins et al., 2018). Larger impacts (such as Apollo Basin in NE SPA) are more likely to excavate through the ejecta blanket and are shaded dark; smaller craters are more likely to re-excavate ejecta blanket materials and are shaded light. The locations of the SPA thorium hotspots (associated with craters Birkeland and Oresme V) are indicated, along with the topographic rim of SPA (Garrick-Bethell & Zuber, 2009). For SPA, the majority of ejecta is expected within the final topographic rim of the basin, in a crescent-shaped distribution centered in the NW quadrant (overlapping with the Th hotspots). The basemap is Lunar Orbiter Laser Altimeter topography over a Lunar Reconnaissance Orbiter Wide Angle Camera mosaic (Smith et al., 2010; Wagner et al., 2015). The light gray dashed rectangle indicates the extent of Figure 3. SPA, South Pole-Aitken Basin.

faulting, slumping, and lateral transport, it is likely that extensive mixing occurred between the ejecta and underlying crustal substrate. This resulted in redistribution and further dilution of mantle-derived ejecta

4. *Emplacement of subsequent (younger) basin ejecta:* Within the SPA interior, it is expected that ~100 m of distal ejecta from subsequent basins was emplaced (Petro & Pieters, 2008). This ejecta is thought to comprise ~50% of the regolith. While this is not a volumetrically significant component compared to the total ejecta volume, it has significant implications for obscuring the surface expression of mantle signatures
5. *Reworking via impact cratering:* SPA is the oldest definitive impact structures on the Moon. Therefore, its ejecta deposit has been subjected to ~4.3 billion years of subsequent impact cratering (including postSPA basin formation). While some of the largest impact structures are large enough to penetrate through and locally remove SPA ejecta (e.g. the 537-km Apollo Basin), younger, smaller craters may instead have churned, redistributed (e.g., Huang et al., 2018; C. Li et al., 2020; Qiao et al., 2019; J. Zhang et al., 2020) and re-exposed ejecta materials from beneath a mixed, diluted regolith. Two such craters

include Birkeland (82 km; Eratosthenian in age (Wilhelms et al., 1987)) and Oresme V (51 km; Upper Imbrian in age (Wilhelms et al., 1987)); see Figure 1

6. *Volcanic resurfacing*: Where present, volcanic resurfacing deposits such as mare basalts, Mons Marguerite (formerly Mafic Mound), and SPACA mask the surface expression of mantle-derived ejecta (Moriarty & Pieters, 2015, 2018; Pieters et al., 2001; Yingst & Head, 1999)

To summarize, SPA formation initially emplaced mantle ejecta in a crescent-shaped distribution centered in the NW. Mantle ejecta was diluted by more than a 1:1 ratio by crustal materials through mixing with crustal ejecta, ballistic sedimentation, and transient cavity collapse (consistent with estimates by Lucey et al., 1998). This deposit was obscured at the surface by volcanic resurfacing, regolith development, and subsequent basin ejecta. In places, mantle ejecta was churned, redistributed, and re-exposed by crater-forming impacts. Basin-scale impacts (such as Apollo) may have penetrated through and locally removed mantle ejecta.

4. Origin of the SPA Thorium Anomaly

Can remnant SPA mantle ejecta be detected in remote sensing data? Although the initial emplacement underwent billions of years of geologic evolution, compositional and mineralogical signatures may persist. In the following sections, we use Lunar Prospector thorium abundance data (Lawrence et al., 2000, 2002b) to investigate the distribution of incompatible elements, which are expected to be concentrated in the uppermost mantle during LMO crystallization. We follow up with Moon Mineralogy Mapper (M^3) (Pieters et al., 2009) analyses to characterize the mineralogy of candidate mantle-derived lithologies, supplementing with additional compositional remote sensing observations.

4.1. The Distribution of Thorium Across SPA

As seen in Lunar Prospector Gamma Ray Spectrometer data (Lawrence et al., 2002b), SPA is associated with a broad enhancement in thorium abundance (Figure 2a). This enhancement exhibits spatial patterns which, considered in geologic context, have been interpreted to support several origin scenarios. As mentioned above, previous interpretations include antipodal ejecta from nearside impact basins (i.e., Imbrium) (Haskin, 1998; Haskin et al., 1998; Lawrence et al., 2000; Stuart-Alexander, 1978; Wieczorek & Zuber, 2001a), lower crust (or upper mantle) exposed by SPA (Garrick-Bethell & Zuber, 2005; Lawrence et al., 2000), and postSPA Mg-suite plutons (Hagerty et al., 2011; Haskin et al., 2004).

4.1.1. Lunar Prospector Th Abundance Observations

Here, we integrate Th abundance data with recent lunar remote sensing data for a detailed understanding of the geologic associations and inferred origin of Th signatures across SPA. The Lunar Prospector team produced several Th abundance maps from different mission phases, with differences in spatial resolution and other properties. We use a 0.5 degree-per-pixel product specifically tailored for geological investigations (Lawrence et al., 2002b). This product is described in further detail in the Data and Methods Appendix (Section 7.2.1).

SPA exhibits a broad enhancement in thorium relative to the farside highlands, confined primarily within the topographic rim of the basin (Figure 2; also noted by Garrick-Bethell & Zuber (2009)). Although Th is slightly elevated throughout the SPA interior relative to the surrounding highlands, the highest abundances are concentrated in NW SPA. Here, two thorium “hotspots” (up to ~6 ppm Th across ~50–100 km regions) are observed in association with craters Birkeland (82 km) and Oresme V (51 km) (Figure 2b) (Garrick-Bethell & Zuber, 2005; Hagerty et al., 2011; Lawrence et al., 2002b, 2000, 2007).

Although Birkeland and Oresme V exhibit the highest Th abundance in the region, several other local Th maxima (“warmspots,” >3 ppm) are also evident throughout the wider crescent-shaped enhancement. Like Birkeland and Oresme V, each of these local Th maxima appear to be associated with impact craters. Several example craters bearing Th “warmspots” include Finsen (72 km), Alder (77 km), Rumford (61 km),

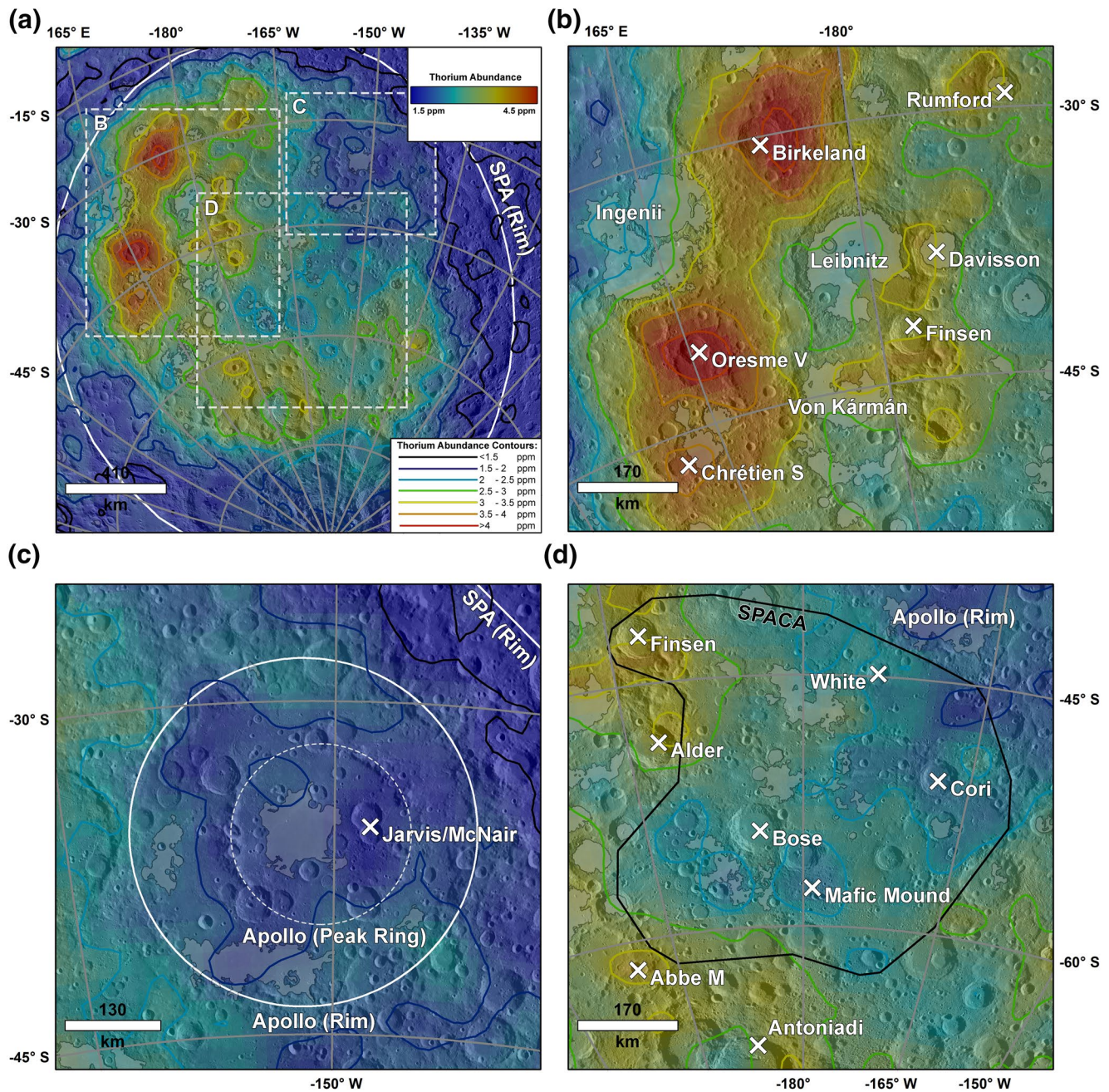


Figure 2. The distribution of thorium across the South Pole–Aitken Basin from Lunar Prospector Gamma Ray Spectrometer data (Lawrence et al., 2002b). (a) The SPA Th anomaly falls primarily within the topographic rim of SPA (white ellipse). Although Th is slightly elevated throughout the SPA interior (relative to the surrounding highlands), the highest abundances are found in NW SPA and appear to be associated with a crescent-shaped distribution reminiscent of the SPA mantle ejecta models (Figure 1). The extent of panels (b–d) are shown by dashed white rectangles. (b) The regional Th distribution around the two “hotspots,” Birkeland, and Oresme V. Although these are the two areas with the highest Th abundance, several other local Th maxima are also evident, associated with craters including Finsen, Alder, Rumford, Davisson, Von Kármán, and Chrétien S. Several local minima are associated with mare basalts (shaded gray), including those within Leibnitz and Ingenii. The western wall of Leibnitz also appears relatively low in Th. (c) Generally, the Apollo Basin is associated with relatively low Th abundance. However, different components of the basin structure exhibit systematic differences in Th abundance. The mare, peak ring, and basin floor exhibit very low Th abundance, while the rim and exterior exhibits slightly elevated Th abundance. (d) Central SPA, dominated by the SPA Compositional Anomaly (SPACA) (Moriarty & Pieters, 2018) exhibits low Th abundance relative to the remainder of the SPA interior. Several distinctive local minima are associated with Mons Marguerite (formerly Mafic Mound) (Moriarty & Pieters, 2015), mare basalts southwest of Bose (Nelson et al., 2014), and smooth plains west and north of Cori. Within SPACA, local Th maxima are observed in association with mare basalts southwest of White. Outside of SPACA, in the primary crescent-shaped Th enrichment, local maxima are observed in association with craters Antoniadi, Alder, and Abbe M. SPA, South Pole–Aitken Basin.

Davisson (87 km), Von Kármán (180 km), Abbe M (29 km), Antoniadis (143 km), and Chrétien S (40 km) (Figures 2b and 2d). However, similar craters in central SPA are not associated with noticeable Th enhancements. These craters include White (39 km), Bose (91 km), and Cori (65 km).

While local Th maxima are associated with craters with diameters on the order of ~50–150 km, pronounced Th minima are associated with larger basins, particularly Apollo (537 km) (Figure 2c). Apollo is associated with relatively low Th abundance (<2.5 ppm). Notably, different components of the basin structure exhibit systematic differences in Th. The peak ring and impact melt sheet (exposed in craters Jarvis and McNair) exhibit local minima in Th abundance (<2 ppm). Apart from the ENE segment, Apollo's rim and exterior exhibits slightly elevated Th abundance (>2 ppm). Similarly, the western wall of Leibnitz (237 km), just to the east of Birkeland and Oresme V, is relatively low in Th.

Local Th minima are also observed in association with volcanic materials across SPA, consistent with previous analyses (e.g., Hagerty et al., 2011). Mare basalts in Apollo, Leibnitz, Ingenii, and southwest of Bose are associated with pronounced local minima in Th abundance (Figure 2). Furthermore, much of the central region of SPA associated with the SPA Compositional Anomaly (SPACA) exhibits Th abundances less than 2.5 ppm (Figure 2d). SPACA is a volcanically resurfaced region that has been interpreted as cryptomare (Whitten & Head, 2015) or unusual nonmare volcanic flooding (Moriarty & Pieters, 2018). Mons Marguerite (formerly Mafic Mound) (Moriarty & Pieters, 2015, 2018), a volcanic construct associated with unusual SPACA magmas, also exhibits a local minimum in Th abundance (<2 ppm).

4.1.2. Apparent Distribution of Th-Bearing Materials and Implications for Origin

Previous interpretations of the Th hotspots associated with Birkeland and Oresme V, including antipodal Imbrium ejecta, consider the hotspots to be discrete, isolated phenomena (e.g., Haskin, 1998; Haskin et al., 1998). However, closer examination demonstrates that these hotspots are not isolated, independent features. Instead, they appear to be associated with a continuous, crescent-shaped Th enrichment. The shape of the Th distribution is reminiscent of SPA ejecta blanket models convolved with subsequent crater and basin formation (Figure 1).

Across much of SPA, local Th maxima are correlated with impact crater structures ~30–150 km in diameter (Figure 2). For craters of this size, excavation depths correspond to approximately 10% of the crater diameter (e.g., Melosh et al., 1989), resulting in material excavated from ~3–15 km. Since this excavated material exhibits a Th-bearing signature, this suggests that Th-bearing deposit is at least ~3–15 km thick. This material has been partially obscured and diluted at the surface, and has been re-exposed by these ~30–150 km impact crater structures.

Larger impact structures such as Apollo (537 km) and Leibnitz (237 km) appear to have excavated through the Th-bearing unit, providing an upper limit on its vertical extent. In Apollo, the Th distribution is systematically correlated with different components of the basin structure representing materials originating at different depths. The rim and ejecta of Apollo appears to contain diluted Th-bearing material (>2 ppm), including a mixture of material from the preimpact surface to the maximum depth of excavation (~50 km). The inner ring and melt sheet represent the deepest materials exposed by the basin (e.g., Cintala & Grieve, 1998), and are very low in Th (<2 ppm). In Leibnitz, the western wall (and craters potentially excavating melt sheet materials) exhibit local minima in Th abundance. Although the thickness of the Th-bearing unit certainly varies across SPA, these observations constrain its maximum thickness to between ~3 and a few tens of km.

In central SPA, 30–150 km craters do not exhibit the same correlation with Th abundance as observed elsewhere in the basin (Figure 2d). This region hosts the thickest portion of the SPA impact melt sheet, and these craters likely excavate its uppermost strata. Evidently, the SPA melt sheet (which originates from greater depths than SPA ejecta) is not notably enriched in Th.

Diverse volcanic deposits across SPA are associated with local minima in thorium abundance (Figure 2). These deposits include mare basalts, pyroclastic emplacements, and unusual volcanic features such as

SPACA and Mons Marguerite. This indicates that the thorium-bearing materials are unlikely to be volcanic in origin, in agreement with previous analyses (e.g., Hagerty et al., 2011).

To summarize, the broad, crescent-shaped elevation in thorium abundance across SPA is similar to the distribution of upper mantle ejecta predicted by three-dimensional models of the SPA-forming impact (Melosh et al., 2017) (Figure 1). After emplacement, this ejecta was redistributed, diluted, and obscured by billions of years of geologic processes including impact cratering, regolith development, and volcanic resurfacing. The observed Th distribution is consistent with the modeled distribution of SPA mantle ejecta convolved through these geologic processes. The Th hotspots at craters Birkeland and Oresme V represent the most recent, relatively pristine re-exposures of this material within SPA.

The broad regional thorium enhancement, exposure from depth in impact craters, and anticorrelation with volcanic materials is inconsistent with several previously proposed models of thorium emplacement such as antipodal ejecta and postSPA magmatism (Haskin et al., 1998; Haskin et al., 2004; Lawrence et al., 2000; Stuart-Alexander, 1978; Wiczorek & Zuber, 2001a). The large lateral (>1,500 km) and vertical (>5 km) extent of thorium-bearing materials cannot be accounted for by antipodal ejecta emplacement or localized magmatic events. The anticorrelation between a diverse volcanic materials (in terms of age and mineralogy) and thorium abundance (Figure 2) further indicates a nonvolcanic origin (Hagerty et al., 2011).

The spatial extent and geologic associations observed in the Th distribution indicate excavation of a widespread, relatively homogeneous unit by the SPA-forming impact. This is consistent with excavation of late-stage ferroan, gabbroic LMO cumulates from the uppermost mantle (i.e., urKREEP), which are expected to host Ti, Th, and other incompatible elements (KREEP). The presence of K is confirmed by Lunar Prospector K elemental abundance (Prettyman et al., 2002) maps (Figure S1), which is spatially correlated with the Th distribution. Further associations with Fe, Ti, and mineralogy are discussed in the following section.

4.2. Mineralogy of Th-Bearing Materials Across SPA

4.2.1. Expected Mineralogy and Near-Infrared Spectral Properties from LMO Crystallization Models

The thorium distribution across SPA is consistent with the distribution of uppermost mantle ejecta predicted by impact models (Figures 1 and 2). If the Th-bearing material does indeed originate from the upper mantle, areas with the highest thorium abundance should exhibit the most distinctive mantle compositional signatures. Although the precise compositional stratigraphy of the upper mantle is unknown due to the uncertainties in the depth of the magma ocean, its bulk composition, and crystallization sequence, LMO crystallization models and experiments typically predict the final product to exhibit a gabbroic, ferroan, ilmenite-bearing mineralogy rich in Th and KREEP (Charlier et al., 2018; Elkins-Tanton et al., 2011; Lin et al., 2017; Rapp & Draper, 2018; Snyder et al., 1992). As noted above, this assemblage is often referred to as “urKREEP.”

A representative example of a reasonable late LMO cumulate assemblage is approximately 30% low-Ca pyroxenes (orthopyroxenes and/or pigeonites), 20% high-Ca,Fe clinopyroxenes, 40% anorthite, and 10% ilmenite/oxides (Elkins-Tanton et al., 2011). However, if plagioclase flotation was efficient, the anorthite content of this assemblage may be significantly lower (Dyger et al., 2017). In either case, the spectral properties of this assemblage can be inferred through comparison with returned lunar samples.

While not an exact match, basaltic rocks returned by the Apollo 15 and 17 missions contain similar minerals in somewhat different ratios. These samples exhibit approximately 25% low-Ca pyroxene, 30% clinopyroxene, 30% anorthite, and 2%–18% ilmenite/oxides (high-Ti basalts 70,017 and 70,035; low-Ti basalts 15,058 and 1,555, Isaacson et al., 2011; Table S1).

From a basic understanding of the near-infrared spectral properties of the constituent minerals (e.g., Burns, 1993), first-order spectral differences between the uppermost mantle assemblage and the Apollo basaltic rocks are straightforward to estimate qualitatively. Compared to typical mare basalts, the predicted urKREEP assemblage (Elkins-Tanton et al., 2011) should exhibit a higher albedo and weaker absorption

bands due to a higher anorthite abundance and lower pyroxene abundance. The urKREEP assemblage should also exhibit slightly shorter-wavelength band centers due to a higher low-Ca pyroxene-to-clinopyroxene ratio.

If plagioclase flotation during LMO crystallization was efficient, this would produce a cumulate layer with little-to-no anorthite content, resulting in stronger absorption bands and lower albedo. However, this may be offset through mixing/dilution by crustal materials. Through several processes discussed in Section 2, mantle-derived SPA ejecta were probably diluted by more than a 1:1 ratio by feldspathic crustal materials. While this lowers the overall pyroxene abundance and results in weaker spectral absorption bands and a higher albedo, it should not significantly affect absorption band centers (Crown & Pieters, 1987). Similarly, space weathering of surface materials will also weaken absorption bands without significantly affecting band centers (Pieters et al., 2000).

In fact, these predicted relationships are exactly what is observed in a comparison between the spectral properties of Th-bearing materials and nearby mare basalts, as detailed in Section 4.2.2 and Figures 3–5. While these schematic qualitative relationships are consistent with a late LMO cumulate origin for Th-bearing materials in SPA, more detailed analyses and eventual sample return are necessary to more precisely constrain the mineralogical properties of these materials.

4.2.2. Comparison with Moon Mineralogy Mapper Observations

4.2.2.1. Regional Trends in M^3 Parameters

The urKREEP spectral properties inferred above are readily recognizable in Moon Mineralogy Mapper (M^3) data. M^3 was a near-infrared spectrometer specifically designed to characterize mineralogical properties of the lunar surface by resolving diagnostic features of the 1 μm and 2 μm absorption bands present in mafic minerals (Pieters et al., 2009). To first order, band depths are related to mafic abundance, while band centers exhibit a systematic relationship with pyroxene composition (Burns, 1993; Klima et al., 2007, 2011). Typically, Mg-rich low-Ca pyroxenes exhibit short-wavelength bands, while Fe, Ca-rich clinopyroxenes exhibit longer-wavelength bands (Klima et al., 2011, 2007; Moriarty & Pieters, 2016). A detailed description of the M^3 data and analysis techniques employed here is given in the Data and Methods Appendix (Section 7.1).

We use the Parabolas and two-part Linear Continuum approach (PLC, developed and validated for use with M^3 data by Moriarty & Pieters, 2016) to derive band depth and center parameters for the 1 and 2 micron absorption bands. These parameter maps are integrated with Th abundance contours, Fe abundance, and Ti abundance data in Figure 3. Further comparisons with K and Ti are provided in Figures S2 and S3.

Mafic abundance across SPA (as inferred from M^3 1 micron band depths) is not strongly correlated with Th abundance (Figure 3a and Figure S3a). The most thorium-rich areas within SPA exhibit only weak pyroxene enhancements relative to nearly mafic-free highlands crustal materials, and are lower in pyroxene abundance than SPA impact melt and resurfaced zones in the basin center (SPACA).

In contrast, pyroxene compositions across SPA (as inferred from M^3 2 micron band centers) appear strongly correlated with Th abundance (Figure 3b and Figure S3b). The zone of highest Th abundance in NW SPA exhibits distinctly longer-wavelength band centers than typical nonvolcanic SPA materials, indicating the presence of Fe,Ca-rich clinopyroxenes. On the lunar surface, it is unusual to observe widespread deposits with these pyroxene compositions outside of mare basalts. This is especially true within SPA, which is otherwise dominated by low-Ca pyroxenes (Lemelin et al., 2019; Moriarty & Pieters, 2018; Ohtake et al., 2014; Tompkins & Pieters, 1999). The inferred pyroxene compositions associated with Th-bearing materials are consistent with the gabbroic, ferroan late LMO assemblage discussed above. The precise mineralogy is not possible to assess with current data due to the highly diluted and mixed nature of this deposit. However, it is apparent that these materials exhibit high abundances of high-Ca pyroxenes.

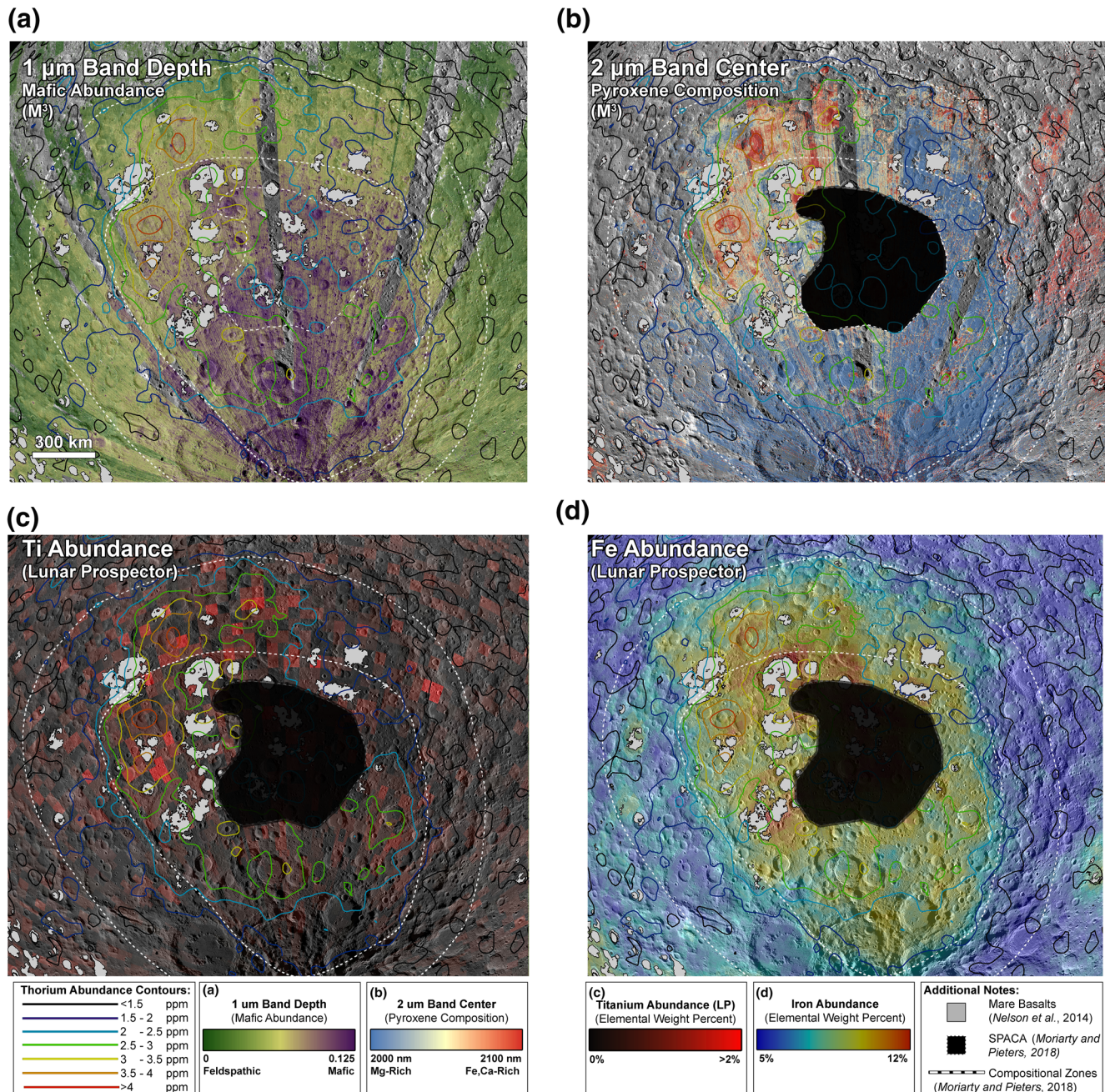


Figure 3. The spatial relationships between thorium (from Lunar Prospector (Lawrence et al., 2002b)), shown as contours on panels (a)–(d) and other compositional and mineralogical properties of SPA basin materials. (a) Mafic abundance from 1 μm band depths in M^3 data. Mare basalts have been masked (Nelson et al., 2014). (b) Pyroxene composition from 2 μm band centers in M^3 data (for pixels with band depths greater than 0.05). Mare basalts and the SPACA resurfaced terrain have been masked for panels b–d (Moriarty & Pieters, 2018; Nelson et al., 2014), as masking volcanically resurfaced terrains emphasizes compositional trends among primary basin materials. (c) Titanium (Prettyman et al., 2002) and (d) FeO abundance (Lawrence et al., 2002) from Lunar Prospector. Basemap for all panels is a LROC WAC mosaic (Wagner et al., 2015). LROC, Lunar Reconnaissance Orbiter Camera; SPA, South Pole-Aitken Basin; SPACA, SPA Compositional Anomaly; WAC, Wide Angle Camera.

4.2.2.2. Relatively Pristine Exposures at Birkeland and Oresme V

Since the Th hotspots associated with craters Birkeland and Oresme V represent the most pristine exposures of thorium-bearing material within SPA, they are the optimal locations to characterize its mineralogy in further detail. M^3 parameter maps for these regions are presented in Figure 4. Spectra and spectral parameters

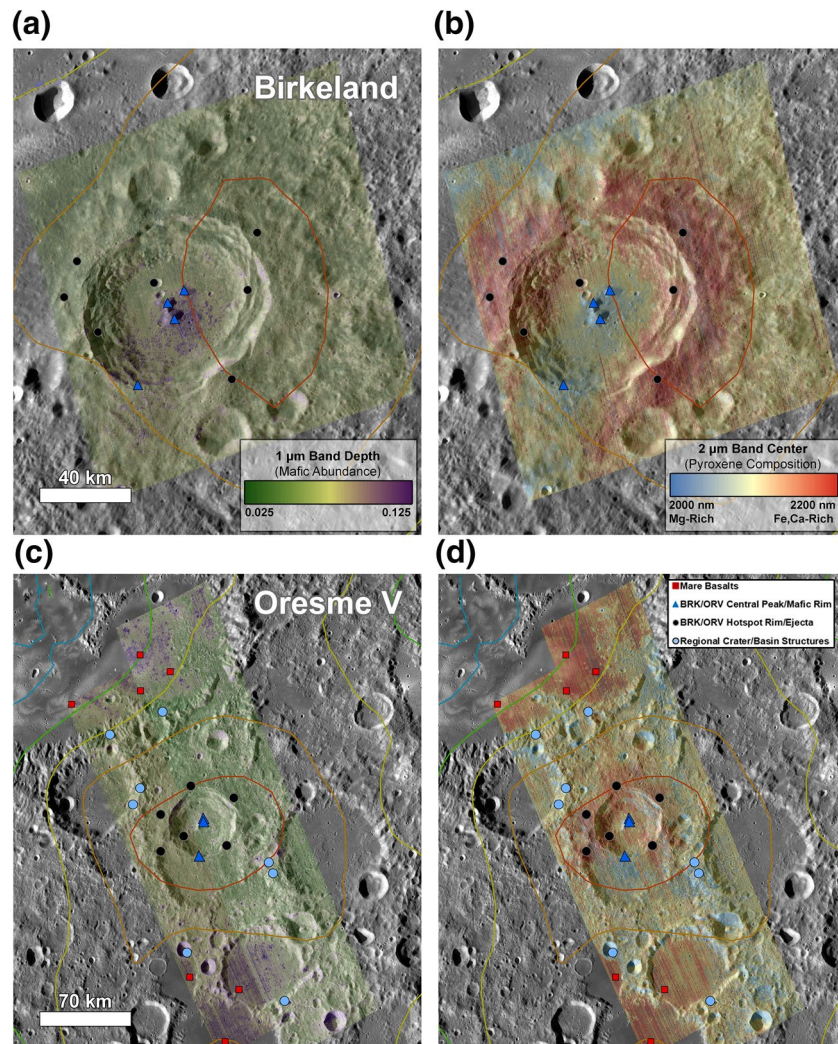


Figure 4. Mafic abundance (A; as per M^3 $1 \mu m$ band depths) and pyroxene compositions (B; as per M^3 $2 \mu m$ band centers) for Birkeland Crater ($30.2^\circ S$, $173.9^\circ E$, 82 km diameter). (C + D) Same for Oresme V ($40.5^\circ S$, $165.6^\circ E$, 51 km diameter). All panels include thorium abundance contours as described in Figure 2.

of the thorium-bearing materials are compared to local mare basalts and low-Ca pyroxene-bearing materials in Figure 5.

From the Th contours in Figure 4, it is clear that the highest Th abundances around Birkeland are associated with its wall/rim, particularly the eastern portion. This part of the crater structure exhibits a relatively low mafic abundance, but the mafic component is dominated by high-Ca,Fe pyroxene compositions (Figures 4a, 4b, 5c and 5d). In contrast, Birkeland's central peak and southwestern wall exhibit lower Th abundances, but higher mafic abundances in association with a Mg-dominated low-Ca pyroxene composition. These mineralogical trends are independently verified by Kaguya Multiband Imager mineral abundance estimates documented by Lemelin et al. (2015, 2019). Oresme V exhibits similar compositional relationships between its wall/rim and central peak (Figures 4c, 4d, 5c and 5d), again, in agreement with Lemelin et al. (2019). On this local scale, the correlation between thorium abundance and a weakly mafic, Ca,Fe-pyroxene-bearing lithology (Figure 4) mirrors the regional pattern observed across NW SPA (Figure 3).

Spectra representing the mineralogical diversity of the hotspot-bearing region were collected from locations indicated in Figure 4, enabling direct comparisons between Th-bearing materials and other regional lithologies (Figure 5). Compared to local mare basalts, the thorium-bearing materials exhibit similar but slightly

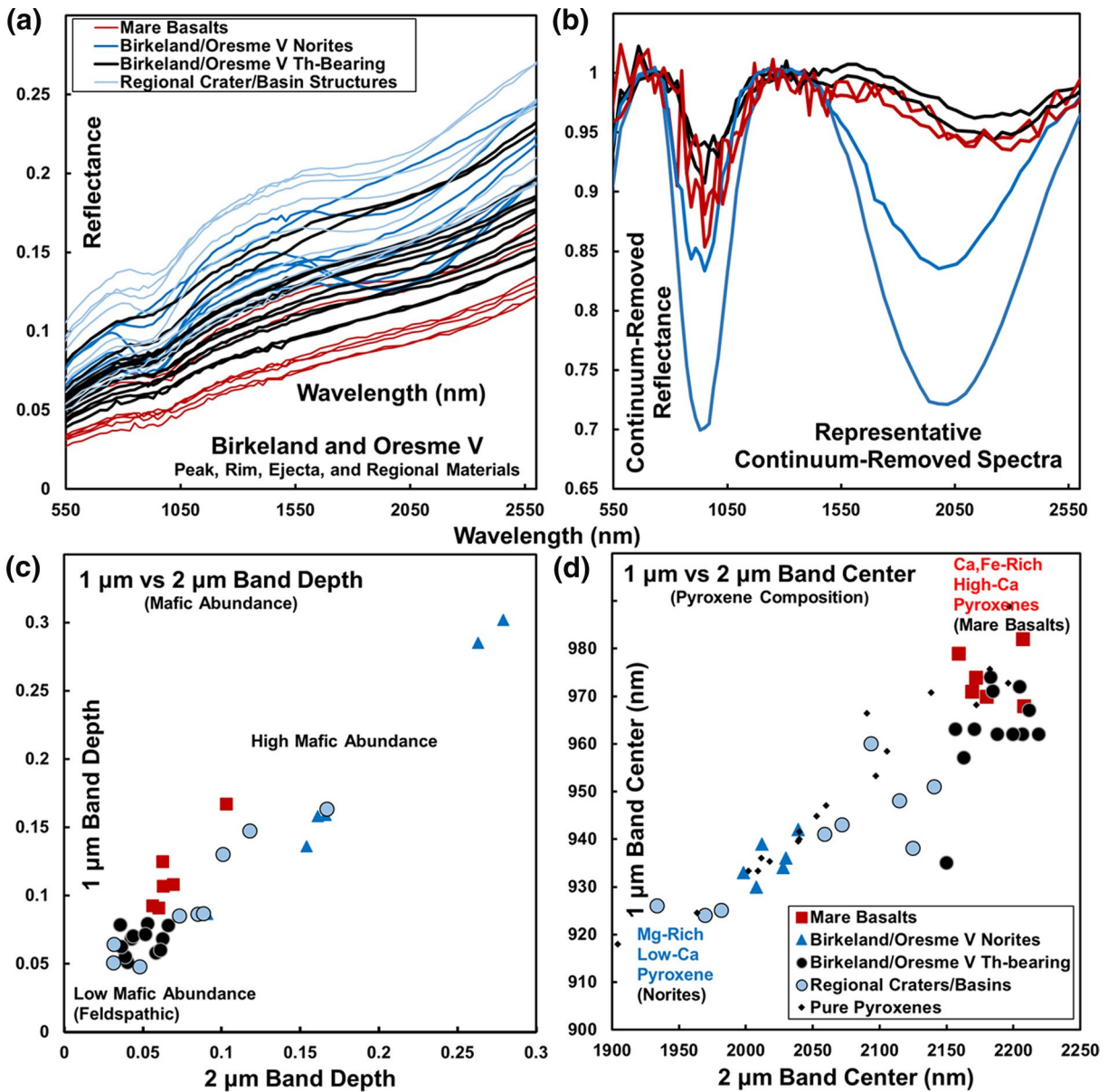


Figure 5. Moon Mineralogy Mapper spectra and spectral parameters demonstrating trends in mineralogical diversity in the region of the SPA thorium hotspots (Figure 3). (a) Reflectance spectra for the locations indicated in Figure 3b. Representative continuum-removed spectra of Th-bearing materials, low-Ca pyroxene-rich materials, and mare basalts. (C + D) Band depths (sensitive to mafic abundance) and centers (sensitive to pyroxene composition) for spectra shown in (a). Spectra, parameter values, and other metadata are provided in a data repository (Moriarty et al., 2020).

shorter-wavelength band centers, indicating average pyroxene compositions slightly lower in Ca and/or Fe. Th-bearing materials are higher in albedo than mare basalts, consistent with a higher abundance of feldspathic crustal minerals.

Interpretation of band depths is complicated by factors such as particle size and optical maturity. However, Th-bearing materials exhibit systematically weaker absorption bands than mare basalts and low-Ca pyroxene-rich central peak materials, which, to first order, suggests a lower mafic content. Overall, Th-bearing materials exhibit higher albedo, weaker absorption bands, and slightly shorter-wavelength band centers compared to local mare basalts. This exactly mirrors the expected differences between Apollo basaltic rocks and late LMO assemblage diluted by crustal materials discussed in Section 4.2.1. While this interpretation

is nonunique, the mineralogical properties of the Th-bearing materials across SPA are consistent with an urKREEP origin.

4.3. Insight from Regional Compositional Observations

The hypothesis that Th-bearing materials across SPA represent ferroan, gabbro-noritic, KREEP- and ilmenite-bearing late LMO cumulates is further supported by elemental and oxide abundance maps. Across SPA, areas exhibiting the highest Th abundances are also associated with elevated FeO (Figure 3d), Ti (Figure 3c), TiO₂ (Figure S3), and K (Figure S2). In conjunction with the observed mineralogy, these observations are consistent with the expected compositional properties of urKREEP.

Intriguingly, Fe in late-stage LMO oxides offers a possible resolution for a previously noted conundrum. Recently, Moriarty and Pieters (2018) observed an unexpected mismatch between M³ band depths and Lunar Prospector Fe abundances across NW SPA. Typically, spectral absorption bands associated with common lunar silicate minerals arise from the presence of Fe in mineral structures (e.g., Burns, 1993). For this reason, Fe abundance is usually correlated with absorption band depths across the lunar surface. However, in NW SPA, elevated Fe abundances are observed without a corresponding enhancement in spectral absorption band depths (Figure 3) (Moriarty & Pieters, 2018). This suggests that much of the Fe across this region is present in nonsilicate materials such as oxides, including Ti-rich ilmenite expected to form late in the LMO crystallization sequence.

As a brief conjecture, the magnitude of magnetic anomalies across SPA exhibits a loose correlation with the Th distribution, and, therefore, the region exhibiting a significant mismatch between M³ band depth and LP Fe abundance (Figure 3, Figure S1). Magnetic anomalies in NW SPA have previously been attributed to subsurface dike swarms (Prurucker et al., 2012) or metallic impactor remnants (Cahill et al., 2014; Wieczorek et al., 2012). However, the results presented here suggest that ferroan uppermost mantle materials ejected by the SPA-forming impact may contribute to the basin's magnetic signature.

4.4. Integration and Origin: urKREEP Versus Mg-Suite

As discussed in Section 4.1, the distribution of Th-bearing materials across SPA is most consistent with an origin as SPA ejecta. The mineralogical and compositional properties of this material are consistent with an urKREEP source. Are there other reasonable hypotheses satisfying these observations?

A previously proposed explanation for the origin of Th-bearing SPA ejecta is Mg-suite magmatism (e.g., Haskin et al., 2004; Hagerty et al., 2011). The Mg-suite encompasses plutonic rocks emplaced within the lunar crust after LMO crystallization (e.g., Shearer et al., 2015). Mg-suite rocks include magnesian gabbro-norites, perhaps consistent with the spectral properties of Th-bearing SPA ejecta. To explain the Th and KREEP component, Hagerty et al. (2011) invoke assimilation from a late LMO cumulate (urKREEP) layer in the uppermost mantle. In this model, the Th signature across SPA is the result of excavated lower crustal materials containing Th-bearing Mg-suite plutons.

This hypothesis is unsatisfactory for both geophysical and compositional reasons. The scenario posed by Hagerty et al. (2011) presumes that the Th signature is the result of relatively shallow excavation from the lower crust. However, recent impact models in conjunction with current crustal thickness measurements suggest that SPA excavated entirely through the crust, excavating material from the upper mantle (Figure 1) (Melosh et al., 2017; Wieczorek et al., 2013). Instead of Th/KREEP assimilated and transported to the crust from the uppermost mantle, it is more likely that SPA ejected material from the upper mantle itself—a much larger reservoir of Th and KREEP.

An urKREEP origin is further supported by the relative lack of Th in SPA impact melt (Figure 2d). If SPA excavation was shallow and the Th signature was due to lower crust Mg-suite plutons, a nonexcavated Th/KREEP-bearing layer in the uppermost mantle is expected (Hagerty et al., 2011). Because the depth of melting exceeds the depth of excavation for basin-scale impacts (e.g., Cintala & Grieve, 1998; Melosh et al., 2017; Potter et al., 2012), SPA impact melt would incorporate this significant reservoir of Th/KREEP. However,

as noted in Section 4.1 and Figure 2d, SPA impact melt is not associated with a Th-bearing signature. This precludes urKREEP as a significant component of SPA impact melt. Instead, our observations are more consistent with complete excavation of mantle-derived urKREEP by SPA formation, with SPA impact melt forming from deeper mantle strata with lower Th and KREEP content.

Compositionally, Mg-suite rocks (including dunites, troctolites, spinel troctolites, Mg-spinels, and gabbro-norites) are notably diverse in mineralogy and Th content, and most are not enriched in Fe ($Mg\# > 60$) or Ti ($< 1 \text{ wt\% Ti}$) (Gross et al., 2020; Gross & Joy, 2016; Roberts et al., 2019; Shearer & Papike, 2005; Shearer et al., 2015; Sun et al., 2017). The mineralogical and compositional diversity of Mg-suite lithologies is not consistent with the broad, relatively uniform compositional signature of the gabbro-noritic, Fe-, Th-, and Ti-bearing SPA ejecta deposit. However, the Fe-, Th-, and Ti-bearing signature (Figure 3, Figure S3) is consistent with an urKREEP origin (Charlier et al., 2018; Elkins-Tanton et al., 2011; Lin et al., 2017; Rapp & Draper, 2018; Snyder et al., 1992). Therefore, a Mg-suite origin for the Th anomaly is compositionally unsatisfactory. This is not to say that Mg-suite plutons were not excavated by the SPA-forming impact; rather, it is unlikely that they represent the primary Th signature observed across SPA.

5. Implications for Lunar Mantle Evolution and Stratigraphy

5.1. Lunar Magma Ocean Crystallization, Overturn, and Thermal Evolution

The distribution and compositional properties of thorium-bearing materials within SPA is consistent with exposure of a ferroan, KREEPy, gabbro-noritic, ilmenite-bearing late LMO assemblage (i.e., urKREEP) from the uppermost lunar mantle (Charlier et al., 2018; Lin et al., 2017; Rapp & Draper, 2018; Snyder et al., 1992). Excavation of such materials by SPA has several important implications for mantle evolution.

First, these observations confirm the presence of indigenous KREEP-bearing mantle material on the lunar farside. This indicates that KREEP-enriched, ilmenite-bearing LMO cumulates were globally distributed early in lunar history, rather than sequestered on the nearside. This is an important observation, as KREEP sequestration on the nearside during LMO evolution has often been invoked to explain the lunar dichotomy in crustal thickness and volcanic properties (Arai et al., 2008; Cadogan, 1974; Gross & Joy, 2016; Loper & Werner, 2002; Wasson & Warren, 1980; Whitaker, 1981). Because SPA excavated KREEP-bearing LMO products, mechanisms other than nearside KREEP sequestration are required to explain these hemispherical differences, unless KREEP sequestration postdated SPA formation (Arkani-Hamed & Pentecost, 2001). Hence, models of hemispheric KREEP sequestration invoking asymmetric LMO crystallization (e.g., Wasson & Warren, 1980; Loper & Werner, 2002) are no longer tenable.

These results also constrain the timing of SPA formation relative to mantle restructuring processes. Since urKREEP was present in SPA ejecta, this dense assemblage could not have fully participated in large-scale gravitational overturn at the time of SPA formation, unless overturn was inefficient in redistributing late magma ocean cumulates (e.g., Zhao et al., 2019). This agrees with petrological models of the SPA impact melt sheet, which demonstrate that the observed impact melt compositions are most consistent with a pre-overturn upper mantle (Hurwitz & Kring, 2014).

Based on the timescale of LMO crystallization and overturn processes suggested by recent numerical models and laboratory experiments, the observation of the ferroan, ilmenite-bearing late LMO assemblage seemingly imposes a tight constraint on the timing SPA formation. Overturn of the ilmenite-bearing late LMO assemblage is thought to be a rapid process, occurring over millions to 10s of Myr (C. Li et al., 2019; Yu et al., 2019; Zhao et al., 2019). Since LMO crystallization is thought to have occurred over 100s of Myr (Borg et al., 2019, 2011; Elkins-Tanton et al., 2011; Gaffney & Borg, 2014; Maurice et al., 2020; Thiemens et al., 2019), it is possible that these dense cumulates sank during LMO crystallization (Dyger et al., 2016; Hess & Parmentier, 1995).

Did SPA form before LMO solidification was complete? In that case, could the thermal state of the lunar lithosphere have preserved a SPA-scale basin (e.g., Trowbridge et al., 2020)? The lower limit on the age of SPA is only loosely determined by crater counting, (e.g., Ivanov et al., 2018). Constraining the timing of

SPA formation through sequential relationships with LMO crystallization processes could provide a tighter constraint, pending confirmation through sample analysis.

Alternatively, has the overturn timescale been underestimated? Did some fraction of urKREEP cumulates not participate in overturn? Or, did large scale overturn not occur? These intriguing questions are important to consider in order to better understand the relationship between SPA formation and mantle evolution. Returning samples of Th-bearing mantle ejecta for analysis in terrestrial laboratories is essential for addressing these fundamental science questions underpinning lunar evolution.

In addition to probing the lunar mantle, SPA formation may have significantly influenced its local thermal evolution. As SPA impact melt does not appear to contain significant Th/KREEP, the SPA-forming impact appears to have completely excavated and removed dense, heat-producing radioactive elements from this region of the uppermost farside mantle. If KREEP contributes to generation of mare basalts by (a) driving mantle overturn and/or (b) providing radiogenic heat that melts the mantle (e.g., Hess & Parmentier, 1995), local removal of KREEP by the SPA-forming impact may have been a contributing factor to the comparative paucity of observable mare basalts in this region.

In fact, the SPA interior exhibits a low degree of mare basalt fill compared to other large lunar basins, as well as several unusual volcanic deposits including SPACA and Mons Marguerite (Moriarty & Pieters, 2015, 2018). The few mare ponds emplaced within SPA exhibit a low Th content, implying that radioactive heating was not a significant factor in their production, in contrast to some nearside basalts (Hagerty et al., 2011).

This effect may not be limited to the SPA interior. It is possible that vigorous localized mantle convection caused by the SPA-forming impact could have stripped Th/KREEP-bearing late LMO cumulates from the uppermost mantle across a wide swath of the lunar farside (Arkani-Hamed & Pentecost, 2001). Such a process could potentially resolve the apparent conflict between the suggested sequestration of KREEP on the nearside with the exposure of KREEP by the SPA-forming impact.

5.2. Stratigraphy of the Upper Mantle and SPA Ejecta Deposit

5.2.1. SPA Target Upper Mantle

The compositional patterns observed across SPA provide insight into the stratigraphy of the crust and upper mantle, as well as the current distribution and stratigraphy of its ejecta deposit.

In basin-scale impacts, the depth of melting greatly exceeds the maximum depth of excavation (Cintala & Grieve, 1998; Potter et al., 2012). In SPA, the depth of melting may have exceeded 300 km, while the maximum depth of excavation was on the order of 100 km (Melosh et al., 2017; Potter et al., 2012).

As detailed in Section 4, SPA ejecta exhibits a gabbroanitic, ferroan lithology enriched in Fe, Ti, K, and Th (and, by proxy, KREEP). In contrast to the gabbroanitic ejecta, SPA impact melt is dominated by low-Ca pyroxenes (Lemelin et al., 2015; Moriarty et al., 2013; Moriarty & Pieters, 2018; Nakamura et al., 2009; Ohtake et al., 2014), and is not associated with Th or Ti. This implies that the impact melt source region had a different bulk composition than the ejecta. Since the lunar crust is primarily feldspathic, this constrains the origin of the Th-bearing materials to a fairly narrow horizon in the uppermost mantle. Considered together, this is direct observational evidence for a stratified crust and upper mantle at the time and location of the SPA-forming impact.

Although the precise depths depend on assumptions and specific parameters in impact and crustal thickness models (Melosh et al., 2017; Potter et al., 2012; Wiczorek et al., 2013), a reasonable, simplified three-layer stratigraphy generalized from these observations includes a ~45 km thick crust (Wiczorek et al., 2013) underlain by up to ~50 km of a ferroan, gabbroanitic, KREEP-, Th-, and Ti-bearing late LMO assemblage (urKREEP). Deeper upper mantle materials (between ~100 and ~300 km) are dominated by low-Ca pyroxenes, as indicated by the SPA impact melt sheet. A stratigraphy consistent with these observations is illustrated schematically in Figure 6a.

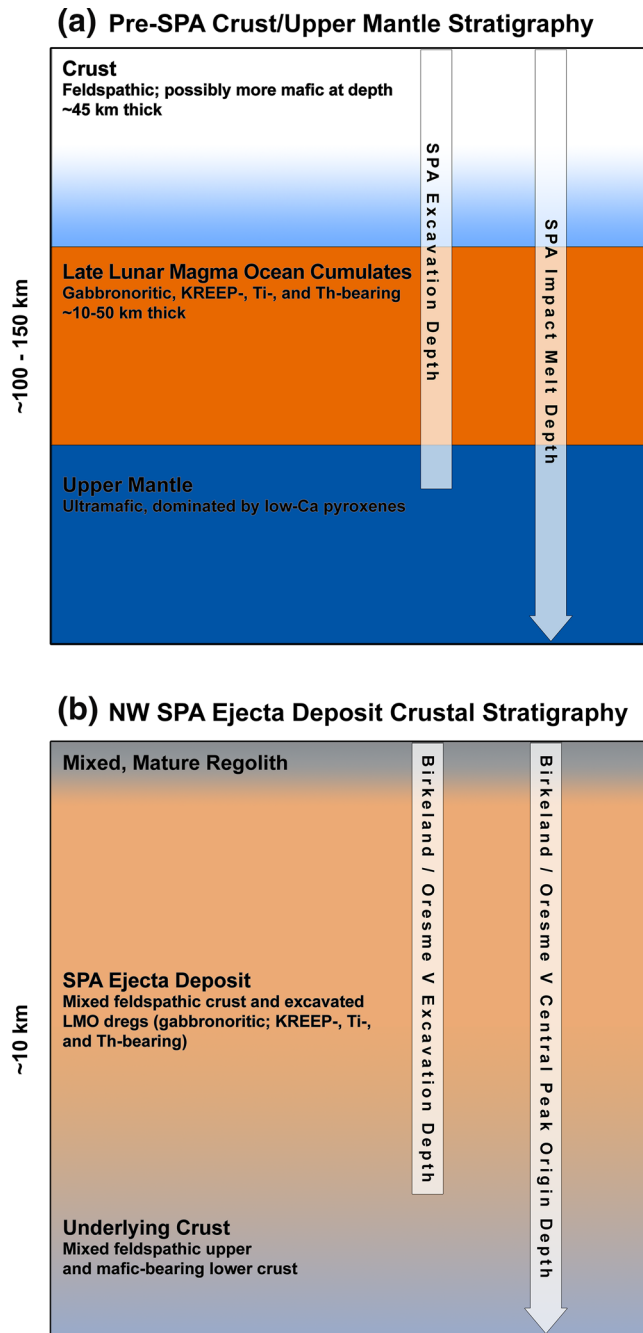


Figure 6. (a) The inferred stratigraphy of the crust and upper mantle at the time and location of SPA formation, consistent with the observed compositional patterns in SPA ejecta and impact melt. An increasing mafic character of the lower crust has been suggested by orbital observations (e.g., Wieczorek & Zuber, 2001b) and central peak compositions of Birkeland and Oresme V, but is not well-constrained globally. (b) The current stratigraphy of the NW SPA ejecta deposit, consistent with the gabbronoritic, Th-bearing rims/ejecta and low-Ca pyroxene-rich central peaks of Birkeland and Oresme V. For (A + B), layer thicknesses are schematic and not to scale. See Section 5.2 for further explanation and justification. SPA, South Pole-Aitken Basin.

Notably, this stratigraphy is inconsistent with a magnesian, olivine- or orthopyroxene-dominated upper mantle at the time and location of SPA formation. Although SPA does not exhibit widespread olivine in remote sensing data (e.g. Melosh et al., 2017; Moriarty & Pieters, 2018; Ohtake et al., 2014), localized detections from Kaguya (Yamamoto et al., 2012) and Chang'E-4's Yutu-2 rover (Gou et al., 2019; Li et al., 2019) have been interpreted to be mantle materials excavated by SPA. However, the Chang'E-4 olivine detections (and claimed mantle origin) have been disputed through further analysis of Yutu-2 in situ data (Hu et al., 2019; Huang et al., 2020) and remote sensing data (Moriarty and Petro, 2020). Given our direct identification of widespread mantle materials lacking a significant olivine component, the most likely origin for the localized olivine detections is Mg suite or other postLMO magmatic products (e.g., Prissel & Gross, 2020).

5.2.2. SPA Ejecta Deposit

While SPA ejecta and impact melt probe the prebasin crust and upper mantle to depths greater than 100 km, the stratigraphy of the SPA ejecta deposit is revealed by subsequent impact events. This stratigraphy is of key scientific interest, as the ejecta deposit includes abundant mantle materials currently accessible at the lunar surface—a valuable target for future sample return missions or in situ analyses (e.g., Jolliff et al., 2017).

Within the Th-bearing SPA ejecta deposit, local Th maxima correspond primarily to impact crater structures ~50–150 km in diameter. This pattern of correlation indicates that the most pristine exposures of Th-bearing materials have been excavated from depth. At the very surface, the compositional and mineralogical signatures of the ejecta deposit have been diluted, seemingly by the development of mixed regolith including local and nonlocal materials. Although diluted, surface materials retain some compositional and mineralogical signatures of excavated urKREEP (Figure 3). This indicates that these materials are indeed widely present at the surface: Lunar Prospector Gamma Ray Spectrometer data are sensitive to ~1 m depths, while M³ spectra measure only the optical surface. Local maxima in Th abundance represent the most pristine re-exposures of SPA ejecta from beneath a mixed and diluted regolith.

Central peak craters are of particular interest for establishing local stratigraphic relationships, as central peak materials originate from greater depths than wall/rim materials (Cintala & Grieve, 1998). Several central peak craters within the SPA ejecta deposit (including Birkeland, Finsen, and Oresme V) exhibit gabbronoritic, Th-bearing materials in their walls/rims, but noritic materials in their central peaks. Since central peaks typically represent the deepest material exposed in complex craters (Cintala & Grieve, 1998), the central peak origin depth establishes an upper limit for the thickness of the SPA ejecta deposit. Based on estimated origin depths for central peak materials from equations published by Cintala and Grieve (1998), central peak materials in Birkeland and Oresme V were uplifted from ~6.5 and ~13 km, respectively. Since SPA ejecta was emplaced on a crustal substrate, the central peaks most likely originate from mixed upper and lower crustal lithologies, which may contain a

noritic component (i.e., Tompkins and Pieters, 1999). This constrains the maximum thickness of the gabbro-noritic SPA ejecta deposit in this vicinity.

This inferred maximum thickness is consistent with the compositional and mineralogical properties of larger impact structures including Leibnitz (237 km) to the east of Birkeland and Oresme V. Leibnitz exhibits noritic, relatively low-Th materials in its walls/rim, indicating that it excavated materials from beneath the SPA ejecta deposit. In NE SPA, the Apollo Basin (537 km) also appears to have excavated through any Th-bearing deposit emplaced by SPA, as its rim, ejecta, and interior exhibit low Th abundances. A stratigraphy consistent with these observations is illustrated schematically in Figure 6b.

6. Conclusions

1. *The thorium anomaly across SPA reflects emplacement of deep SPA ejecta:* Integrating elemental abundances with mineralogy, impact models, and geologic context, it was demonstrated that the Th enhancement associated with the South Pole-Aitken Basin is the result of SPA ejecta sourced from ~50–100 km beneath the preimpact surface. The pattern of Th abundance across SPA reflects the distribution of the SPA ejecta blanket convolved through ~4 billion years of subsequent geologic processing including impact cratering, volcanic resurfacing, and regolith development. These observations are inconsistent with previous hypotheses for the SPA Th anomaly including localized volcanic emplacements, Mg-suite intrusions, and antipodal basin ejecta
2. *Thorium-bearing materials within SPA represent uppermost mantle ejecta:* The SPA ejecta deposit exhibits a gabbro-noritic mineral assemblage, with elevated K, Th, Fe, and Ti abundances (and, by proxy, KREEP) relative to the farside highlands. The observed mineralogical and compositional properties are consistent with the compositions of late-stage lunar magma ocean cumulates predicted by LMO crystallization models (i.e., urKREEP)
3. *Together, compositional patterns in SPA ejecta and impact melt provide evidence for a stratified ancient upper mantle:* SPA impact melt, sourced from greater depths than ejected urKREEP, is dominated by low-Ca pyroxenes and is relatively low in Th. Evidently, urKREEP was confined to a narrow horizon in the uppermost mantle and underlain by a low-Ca pyroxene-dominated layer. This is direct evidence for a stratified upper mantle at the time and place of SPA formation
4. Excavation of urKREEP by SPA requires that KREEP was distributed globally during LMO crystallization, rather than sequestered beneath the nearside. Therefore, if KREEP sequestration is required to explain the divergent volcanic histories of the nearside and farside, sequestration must have occurred after the SPA-forming impact
5. The timing and/or participation of urKREEP in cumulate mantle overturn is constrained by the presence of KREEP in SPA ejecta. These observations imply that SPA formation occurred before large-scale downwelling of dense LMO upper mantle products. Because this downwelling is thought to occur during or shortly after LMO crystallization (within ~10 Myr), this places tight constraints on the timing of SPA formation relative to this sequence. Alternatively, this may reveal an underestimate in the timescale of cumulate mantle overturn, or imply that overturn did not occur or was not completely efficient in redistributing and sequestering late magma ocean cumulates in the deep lunar interior
6. The current stratigraphy of the SPA mantle ejecta deposit is revealed by integrated remote sensing data. Impact craters ~30–150 km in diameter within the SPA ejecta deposit re-expose Th-bearing materials from beneath a mixed and diluted regolith layer, and provide insight into its stratigraphy. The most pristine exposures of SPA mantle ejecta correspond to craters Birkeland and Oresme V. The walls and rims of these craters are associated with distinctly gabbro-noritic mineralogies and local maxima in Th content. Their central peaks uplift low-Ca pyroxene-dominated, low-Th material from depth, constraining the thickness of SPA ejecta to ~5–10 km in this region. This constraint is consistent with the observations of larger impact structures such as Apollo and Leibnitz, which appear to have completely excavated through the Th-bearing, gabbro-noritic SPA ejecta deposit to expose low-Th noritic materials
7. Mantle materials ejected by SPA and preserved at the surface are high-priority science targets for future missions and analyses. Formation of the South Pole-Aitken Basin is among the most ancient and important events in lunar history. Not only did it affect the thermal and chemical evolution of the lunar

mantle, but it preserved heterogeneous mantle materials on the lunar surface in the form of ejecta and impact melt. Sampling these materials is critical to validating our interpretations, as well as addressing outstanding lunar science questions regarding the formation and evolution of the lunar crust and interior. Furthermore, ejected impact melt likely recorded the age of SPA, a keystone for unraveling solar system geochronology. As we enter into a new age of international and commercial lunar exploration, these mantle materials at the lunar surface must be considered among the highest-priority targets for the advancement of planetary science.

7. Appendix: Data and Methods

7.1. Moon Mineralogy Mapper Analyses

Moon Mineralogy Mapper (Pieters et al., 2009) data provide the highest spatial- and spectral-resolution mineralogical data for the lunar surface and are therefore ideally suited for characterizing compositional diversity. For these analyses, we use Planetary Data System-released Level 2 global-mode M^3 reflectance images, which have been thermally and photometrically corrected and normalized to a standard viewing geometry ($i = 30^\circ$, $e = 0^\circ$, $g = 30^\circ$) (Besse et al., 2013). These data have a nominal spatial resolution of 140–280 m per pixel and spectral resolution of 20–40 nm per channel from 540 to 3,000 nm (Boardman et al., 2011; Pieters et al., 2009). A further ground truth correction based on Apollo soils was applied (Isaacson et al., 2013). Nominal signal-to-noise was between 100 and 400, depending on latitude, and cross-track and field-of-view spectral uniformity was $>90\%$ (Green et al., 2011).

However, observing conditions (such as phase angle, solar illumination, detector temperature, spacecraft altitude, etc.) varied throughout the mission, affecting spatial resolution as well as detector response (Boardman et al., 2011). To account for these changing conditions, M^3 data are divided into several convenient optical periods (OPs). Calibration efforts such as a photometric correction to a standard viewing geometry (Besse et al., 2013) were undertaken to produce a uniform data set, but small and often systematic artifacts persist between the OPs. While M^3 achieved nearly complete coverage of SPA, the coverage of the basin is divided between several OPs. OP2C offers the broadest coverage of SPA. Additional coverage is also available in OP1A, OP1B, and OP2A.

Spectral variations across the South Pole-Aitken Basin are dominated by differences in the abundance and composition of pyroxenes (Moriarty & Pieters, 2018). Therefore, differences in mineralogy across SPA are well-captured by differences in albedo and the diagnostic properties (depth and center) of the 1 μm and 2 μm absorption bands. To first order, absorption band depths increase with pyroxene abundance, although factors such as optical maturity also affect band depths (Burns, 1993). Band centers are sensitive to pyroxene composition. Mg-rich pyroxenes exhibit short-wavelength 1 μm and 2 μm bands; band centers shift to longer wavelengths with increasing Fe and Ca content (Klima et al., 2007, 2011).

Maps of these mineralogically sensitive parameters were generated from M^3 data using the **Parabolas** and two-part **Linear Continuum** (PLC) method, which was developed and validated for use with M^3 data by Moriarty and Pieters (2016). The PLC approach performs parabola fits to the 1 μm and 2 μm absorption bands after a two-part linear continuum is calculated (from three tiepoints) and removed. The code is optimized to derive detailed mineralogical information from M^3 images while minimizing the contribution of instrument artifacts. Although the error in these calculations varies with signal-to-noise (which is dependent on a number of factors including latitude, surface albedo, detector temperature, etc.), a serviceable rule-of-thumb is that the PLC method derives band centers from M^3 data accurate to less than the width of one spectral channel (20 nm for the 1 μm band, 40 nm for the 2 μm band). Pixels exhibiting anomalously high noise impacting band centers were discarded. Compared to the Modified Gaussian Model (Sunshine et al., 1990), PLC band center measurements for pure pyroxenes measured in the laboratory exhibit a ~ 6 nm root-mean-square error for the 1 micron band and a ~ 17 nm root-mean-square error for the 2 micron band (Moriarty & Pieters, 2016). This falls within the range of noise-based errors. PLC-derived band depths are conservatively estimated to be accurate to within 0.025.

Regional analyses were performed with PLC-generated parameter maps derived from M^3 global mosaics produced by Boardman et al. (2011) (Figures 3c and 3d). These mosaics have a 10X lower spatial resolution

than full-resolution global-mode M^3 data, but higher signal-to-noise. Detailed local analyses of the thorium hotspots were performed with M^3 images M3G20090720T003411 + M3G20090720T043741 (for Birkeland) and M3G20090720T173631 + M3G20090720T140000 (for Oresme V) (Figures 4a–4d). After parameter maps were generated using the PLC technique (using the Interactive Data Language programming language), M^3 images were georeferenced (using M^3 L1B location file backplanes available on the Planetary Data System) for integration with other lunar remote sensing data in ArcMap. Because band center measurements are susceptible to artifacts from low signal-to-noise in pixels with weak absorption bands, band center values are only shown for pixels with band depths greater than 0.05.

Spectra shown in Figure 4e are 3×3 pixel averages from full-resolution M^3 global mode images. The locations of these spectra are indicated in Figures 4a–4d. Band center and band depth values reported in Figure 4f and 4g are derived from these average spectra using the PLC method. Band center values are compared to those of a suite of pure pyroxenes (Klima et al., 2011, 2007; Moriarty & Pieters, 2016).

7.2. ArcMap Integration of Remote Sensing Data and Impact Models

Integration of M^3 mineralogical data, Lunar Prospector thorium abundance, additional remote sensing data, and impact model results was performed in ArcGIS 10.3.1. Maps shown throughout the text are in an orthographic projection centered near Mons Marguerite (formerly Mafic Mound) in central SPA (58°S, 163°W). A short description of each data set is provided in the following subsections.

7.2.1. Lunar Prospector Elemental and Oxide Abundances

Thorium elemental abundance data was obtained from the Lunar Prospector Reduced Spectrometer Data Special Products repository on the Planetary Data System Geoscience Node, hosted by Washington University in St. Louis. The Th abundance data used here is a special product generated by the Lunar Prospector team, specifically designed to maximize spatial resolution for the purposes of investigating correlations with surface geological features (Lawrence et al., 2002b). These data have a FWHM spatial resolution of ~ 62 km per pixel and are mapped at 0.5° per pixel, and were obtained using a technique leveraging both low- and high-altitude Lunar Prospector data and smoothed using a two-dimensional Gaussian function with a FWHM of 62 km (Lawrence et al., 2002b). This technique highlights Th enhancements and high-contrast interfaces, sharpening small-area features (Lawrence et al., 2002b). Thorium abundance data from the low-altitude portion of the mission are associated with uncertainties less than 15% (Lawrence et al., 2000). Using ArcMap, 0.5 ppm thorium abundance contour lines were generated to emphasize local variation within the context of other lunar remote sensing data. While more recent Th abundance maps corrected using Apollo samples are quantitatively more accurate (Prettyman et al., 2006), the spatial resolution is lower (at best, 2° per pixel). The 0.5° per pixel product used here (Lawrence et al., 2002b) is better-suited for the geospatial nature of our analyses, i.e. demonstrating spatial correlation with other M^3 data and other remote sensing analyses.

FeO abundance maps from Lunar Prospector have a spatial resolution of 0.5° per pixel and are described by Lawrence et al. (2002). Lunar Prospector elemental Ti and K abundance maps have a spatial resolution of 2° (binned at 60 km) per pixel and are described by Prettyman et al. (2002).

7.2.2. Lunar Reconnaissance Orbiter Camera Imagery

The basemap image mosaic used throughout this paper is the Global Morphologic Map from the Lunar Reconnaissance Orbiter Camera (LROC) Wide Angle Camera (WAC) (Speyerer et al., 2011; Wagner et al., 2015). The mosaic was constructed from the 643 nm band and has a spatial resolution of 100 meters per pixel. The mosaic was generated, map-projected (Speyerer et al., 2016), and photometrically corrected (Sato et al., 2014) by the LROC team.

7.2.3. Lunar Orbiter Laser Altimeter Topography

Topography data is from the Lunar Orbiter Laser Altimeter (LOLA). The 256 pixel per degree digital elevation model has a spatial resolution of 118.45 meters per pixel.

7.2.4. Mantle-Derived Ejecta Deposit Model

The distribution of uppermost mantle-derived ejecta postSPA formation is derived from three-dimensional iSALE impact hydrocode simulations conducted by coauthor Kendall and previously published by Melosh et al. (2017). Although several impact scenarios were modeled, we choose the nominal case, the model parameters of which include a 200 km impactor diameter and 45° impact angle. These parameters result in an 850 km transient cavity diameter and a maximum depth of ejecta of 105 km. The model uses cubic cells with side lengths of 10 km.

Assuming a crustal thickness of 45 km (based on GRAIL estimates (Wieczorek et al., 2013)), we consider ejecta originating from depths between 45 km and 105 km to represent mantle-derived ejecta. The distribution of this mantle-derived ejecta was extracted from the model results and imported into ArcMap for direct comparison with remote sensing data.

7.2.5. Additional Data

Crater locations and diameters were obtained from the Lunar Orbiter Laser Altimeter Large Lunar Crater Catalog, which includes most lunar craters 20 km or larger in diameter (Head et al., 2010; Kadish et al., 2011). This catalog may underrepresent the number of craters 20–50 km in diameter by 10%–50%, with better representation at larger crater diameters (Robbins et al., 2018). This underrepresentation of ~20 km craters does not affect our interpretations.

Lunar mare boundaries were mapped by Nelson et al. (2014) using LROC WAC and Clementine data. LROC TiO₂ maps were produced by Sato et al. (2017).

The boundary for the South Pole-Aitken Compositional Anomaly was mapped by Moriarty and Pieters (2018). SELENE Lunar Magnetometer are as described by Tsunakawa et al. (2010).

Data Availability Statement

All data and methods needed to understand, evaluate, and build upon this research are publicly available and documented through a combination of publicly accessible repositories and prior publications. Sources include:

- Moon Mineralogy Mapper Level 2 reflectance data (available through the Planetary Data System Imaging Node: <https://pds-imaging.jpl.nasa.gov/volumes/m3.html>)
- M³ parameter maps were generated from Level 2 reflectance data using the Parabolas and two-part Linear Continuum (PLC) method (Moriarty & Pieters, 2016)
- Spectral absorption band values for pure pyroxenes (Klima et al., 2007, 2011)
- Lunar Prospector thorium, iron, titanium, and potassium abundance maps (https://pds-geosciences.wustl.edu/missions/lunarp/reduced_special.html)
- Lunar Reconnaissance Orbiter Camera Global Morphological Map (Speyerer et al., 2011) and TiO₂ abundances (Sato et al., 2017)
- Lunar Orbiter Laser Altimeter topography data (<https://pds-geosciences.wustl.edu/missions/lro/lola.htm>.)
- Mantle-derived SPA ejecta model (Melosh et al., 2017)
- LOLA Large Lunar Crater Catalog (Head et al., 2010; Kadish et al., 2011)
- Lunar mare boundaries (Nelson et al., 2014)
- South Pole-Aitken Compositional Anomaly boundaries (Moriarty & Pieters, 2018)

- Lunar sample compositional data from the Lunar Rock and Mineral Characterization Consortium (Isaacson et al., 2013)
- Lunar Magma Ocean crystallization model compositional estimates (Elkins-Tanton et al., 2011)
- SELENE Lunar Magnetometer data (Tsunakawa et al., 2010)
- Derived data products including band depths, band centers, and spectra are available through a FAIR-enabling data repository (Moriarty et al., 2020)

Acknowledgments

This analysis benefitted from discussions with Carle Pieters, Jay Melosh, and Brad Jolliff. The authors thank reviewers Myriam Lemelin and Katherine Joy and Editors David Trang and Laurent Montesi for feedback that has improved the quality of the manuscript. To the best knowledge of the authors, there are no real or perceived financial or affiliation conflicts of interests for any author. Significant portions of this work were conducted by the TREX team and supported by the National Aeronautics and Space Administration (NASA) through the Solar System Exploration Virtual Institute 2016 (SSERV12016) Cooperative Agreement (NNH16ZDA001N).

References

Arai, T., Takeda, H., Yamaguchi, A., & Ohtake, M. (2008). A new model of lunar crust: Asymmetry in crustal composition and evolution. *Earth Planets and Space*, 60(4), 433–444. <https://doi.org/10.1186/BF03352808>

Arkani-Hamed, J., & Pentecost, A. (2001). On the source region of the lunar mare basalt. *Journal of Geophysical Research*, 106(E7), 14691–14700. <https://doi.org/10.1029/2000JE001395>

Besse, S., Sunshine, J., Staid, M., Boardman, J., Pieters, C., Guasqui, P., & Li, J. Y. (2013). A visible and near-infrared photometric correction for Moon Mineralogy Mapper (M3). *Icarus*, 222(1), 229–242. <https://doi.org/10.1016/j.icarus.2012.10.036>

Boardman, J. W., Pieters, C. M., Green, R. O., Lundeen, S. R., Varanasi, P., Nettles, J., et al. (2011). Measuring moonlight: An overview of the spatial properties, lunar coverage, selenolocation, and related Level 1B products of the Moon Mineralogy Mapper. *Journal of Geophysical Research*, 116, E6. <https://doi.org/10.1029/2010JE003730>

Borg, L. E., Connelly, J. N., Boyet, M., & Carlson, R. W. (2011). Chronological evidence that the Moon is either young or did not have a global magma ocean. *Nature*, 477, 70–73. <https://doi.org/10.1038/nature10328>

Borg, L. E., Gaffney, A. M., et al. (2019). Isotopic evidence for a young lunar magma ocean. *Earth and Planetary Science Letters*, 523, 115706. <https://doi.org/10.1016/j.epsl.2019.07.008>

Borst, A. M., Foing, B. H., Davies, G. R., & Van Westrenen, W. (2012). Surface mineralogy and stratigraphy of the lunar South Pole-Aitken basin determined from Clementine UV/VIS and NIR data. *Planetary and Space Science*, 68(1), 76–85. <https://doi.org/10.1016/j.pss.2011.07.020>

Boukaré, C.-E., Parmentier, E.M., Parman, S.W. (2018). Timing of mantle overturn during magma ocean solidification. *Earth and Planetary Science Letters*, 491, 216–225. <https://doi.org/10.1016/j.epsl.2018.03.037>

Buck, W. R., & Toksoz, M. N. (1980). The bulk composition of the Moon based on geophysical constraints. In *Lunar and Planetary Science Conference Proceedings* (Vol. 11, pp. 2043–2058).

Burns, R. G. (1993). *Mineralogical applications of crystal field theory* (Vol. 5). Cambridge, MA: Cambridge University Press.

Cadogan, P. H. (1974). Oldest and largest lunar basin?. *Nature*, 250(5464), 315–316. <http://doi.org/10.1038/250315a0>

Cahill, J. T., Hagerty, J. J., Lawrence, D. J., Klima, R. L., & Blewett, D. T. (2014). Surveying the South Pole-Aitken basin magnetic anomaly for remnant impactor metallic iron. *Icarus*, 243, 27–30. <https://doi.org/10.1016/j.icarus.2014.08.035>

Cahill, J. T. S., Lucey, P. G., & Wieczorek, M. A. (2009). Compositional variations of the lunar crust: Results from radiative transfer modeling of central peak spectra. *Journal of Geophysical Research*, 114, E9. <https://doi.org/10.1029/2008JE003282>

Charlier, B., Grove, T. L., Namur, O., & Holtz, F. (2018). Crystallization of the lunar magma ocean and the primordial mantle-crust differentiation of the Moon. *Geochimica et Cosmochimica Acta*, 234, 50–69. <https://doi.org/10.1016/j.gca.2018.05.006>

Chen, J., Ling, Z., Qiao, L., He, Z., Xu, R., Sun, L., et al. (2020). Mineralogy of Chang'e-4 landing site: preliminary results of visible and near-infrared imaging spectrometer. *Information Sciences*, 63(140903), 1–140903. <https://doi.org/10.1007/s11432-019-2768-1>

Cintala, M. J., & Grieve, R. A. (1998). Scaling impact melting and crater dimensions: Implications for the lunar cratering record. *Meteoritics & Planetary Science*, 33(4), 889–912. <https://doi.org/10.1111/j.1945-5100.1998.tb01695.x>

Crites, S. T., & Lucey, P. G. (2015). Revised mineral and Mg# maps of the Moon from integrating results from the Lunar Prospector neutron and gamma-ray spectrometers with Clementine spectroscopy. *American Mineralogist*, 100(4), 973–982. <https://doi.org/10.2138/am-2015-4874>

Crown, D. A., & Pieters, C. M. (1987). Spectral properties of plagioclase and pyroxene mixtures and the interpretation of lunar soil spectra. *Icarus*, 72(3), 492–506. [https://doi.org/10.1016/0019-1035\(87\)90047-9](https://doi.org/10.1016/0019-1035(87)90047-9)

Dygart, N., Hirth, G., & Liang, Y. (2016). A flow law for ilmenite in dislocation creep: Implications for lunar cumulate mantle overturn. *Geophysical Research Letters*, 43(2), 532–540. <https://doi.org/10.1002/2015GL066546>

Dygart, N., Lin, J. F., Marshall, E. W., Kono, Y., & Gardner, J. E. (2017). A low viscosity lunar magma ocean forms a stratified anorthitic flotation crust with mafic poor and rich units. *Geophysical Research Letters*, 44(22), 11–282. <https://doi.org/10.1002/2017GL075703>

Elardo, S. M., Draper, D. S., & Shearer, C. K., Jr (2011). Lunar Magma Ocean crystallization revisited: Bulk composition, early cumulate mineralogy, and the source regions of the highlands Mg-suite. *Geochimica et Cosmochimica Acta*, 75(11), 3024–3045. <https://doi.org/10.1016/j.gca.2011.02.033>

Elardo, S. M., Laneuville, M., McCubbin, F. M., & Shearer, C. K. (2020). Early crust building enhanced on the Moon's nearside by mantle melting-point depression. *Nature Geoscience*, 13(5), 339–343. <https://doi.org/10.1038/s41561-020-0559-4>

Elkins-Tanton, L. T., Burgess, S., & Yin, Q. Z. (2011). The lunar magma ocean: Reconciling the solidification process with lunar petrology and geochronology. *Earth and Planetary Science Letters*, 304(3–4), 326–336. <https://doi.org/10.1016/j.epsl.2011.02.004>

Evans, A. J., Hanna, J. C. A., Head, J. W., Soderblom, J. M., Solomon, S. C., & Zuber, M. T. (2018). Reexamination of early lunar chronology with GRAIL data: Terranes, basins, and impact fluxes. *Journal of Geophysical Research: Planets*, 5(4), 313. <http://doi.org/10.1029/2017JE005421>

Gaffney, A. M., & Borg, L. E. (2014). A young solidification age for the lunar magma ocean. *Geochimica et Cosmochimica Acta*, 140, 227–240. <https://doi.org/10.1016/j.gca.2014.05.028>

Garrick-Bethell, I., & Zuber, M. T. (2005). An indigenous origin for the South Pole Aitken basin thorium anomaly. *Geophysical Research Letters*, 32. <https://doi.org/10.1029/2005GL023142>

Garrick-Bethell, I., & Zuber, M. T. (2009). Elliptical structure of the lunar South Pole-Aitken basin. *Icarus*, 204(2), 399–408. <https://doi.org/10.1016/j.icarus.2009.05.032>

Gou, S., Di, K., Yue, Z., Liu, Z., He, Z., Xu, R., et al. (2019). Lunar deep materials observed by Chang'e-4 rover. *Earth and Planetary Science Letters*, 528, 115829. <https://doi.org/10.1016/j.epsl.2019.115829>

- Green, R. O., Pieters, C., Mourouls, P., Eastwood, M., Boardman, J., Glavich, T., et al. (2011). The Moon Mineralogy Mapper (M3) imaging spectrometer for lunar science: Instrument description, calibration, on-orbit measurements, science data calibration and on-orbit validation. *Journal of Geophysical Research: Planets*, 116, E10. <https://doi.org/10.1029/2011JE003797>
- Gross, J., Hilton, A., Prissel, T. C., Setera, J. B., Korotev, R. L., & Calzada-Diaz, A. (2020). Geochemistry and petrogenesis of Northwest Africa (NWA) 10401: A new type of the Mg-suite rocks?. *Journal of Geophysical Research: Planets*, e2019JE006225. <https://doi.org/10.1029/2019JE006225>
- Gross, J., & Joy, K. H. (2016). Evolution, lunar: From magma ocean to crust formation. In Cudnik (Ed.), *Encyclopedia of lunar science*. Springer International Publishing AG 2016 B, Basel, Switzerland: Encyclopedia of Lunar Science. https://doi.org/10.1007/978-3-319-05546-6_39-1
- Hagerty, J. J., Lawrence, D. J., & Hawke, B. R. (2011). Thorium abundances of basalt ponds in South Pole-Aitken basin: Insights into the composition and evolution of the far side lunar mantle. *Journal of Geophysical Research*, 116. <https://doi.org/10.1029/2010JE003723>
- Harada, Y., Goossens, S., Matsumoto, K., Yan, J., Ping, J., Noda, H., & Haruyama, J. (2014). Strong tidal heating in an ultralow-viscosity zone at the core–mantle boundary of the Moon. *Nature Geoscience*, 7(8), 569–572. <https://doi.org/10.1038/ngeo2211>
- Haskin, L. A. (1998). The Imbrium impact event and the thorium distribution at the lunar highlands surface. *Journal of Geophysical Research: Planets*, 103(E1), 1679–1689. <https://doi.org/10.1029/97JE03035>
- Haskin, L. A., Korotev, R. L., Rockow, K. M., & Jolliff, B. L. (1998). The case for an Imbrium origin of the Apollo thorium-rich impact-melt breccias. *Meteoritics & Planetary Science*, 33, 959–975. <https://doi.org/10.1111/j.1945-5100.1998.tb01703.x>
- Haskin, L. A., McKinnon, W. B., Benner, L. A. M., & Jolliff, B. L. (2004). Thorium anomalies in the NW quadrant of the South Pole-Aitken Basin. In *Lunar and Planetary Science Conference* (Vol. 35) Houston, TX: LPI.
- Head, J. W., Fassett, C. I., Kadish, S. J., Smith, D. E., Zuber, M. T., Neumann, G. A., & Mazarico, E. (2010). Global distribution of large lunar craters: Implications for resurfacing and impactor populations. *Science*, 329, 1504–1507. <https://doi.org/10.1126/science.1195050>
- Hess, P. C., & Parmentier, E. M. (1995). A model for the thermal and chemical evolution of the Moon's interior: Implications for the onset of mare volcanism. *Earth and Planetary Science Letters*, 134(3–4), 501–514. [https://doi.org/10.1016/0012-821X\(95\)00138-3](https://doi.org/10.1016/0012-821X(95)00138-3)
- Huang, J., Xiao, Z., Flahaut, J., Martinot, M., Head, J., Xiao, X., et al. (2018). Geological characteristics of Von Kármán crater, northwestern south pole-Aitken Basin: Chang'E-4 landing site region. *Journal of Geophysical Research: Planets*, 123(7), 1684–1700. <https://doi.org/10.1029/2018JE005577>
- Huang, J., Xiao, Z., Xiao, L., Horgan, B., Hu, X., Lucey, P., et al. (2020). Diverse rock types detected in the lunar South Pole–Aitken Basin by the Chang'E-4 lunar mission. *Geology*. <https://doi.org/10.1130/G47280.1>
- Hu, X., Ma, P., Yang, Y., Zhu, M. H., Jiang, T., Lucey, P. G., et al. (2019). Mineral abundances inferred from in situ reflectance measurements of Chang'E-4 landing site in South Pole-Aitken Basin. *Geophysical Research Letters*, 46(16), 9439–9447. <https://doi.org/10.1029/2019GL084531>
- Hurwitz, D. M., & Kring, D. A. (2014). Differentiation of the South Pole–Aitken basin impact melt sheet: Implications for lunar exploration. *Journal of Geophysical Research: Planets*, 119(6), 1110–1133. <https://doi.org/10.1002/2013JE004530>
- Isaacson, P. J., Basu Sarbadhikari, A., Pieters, C. M., Klima, R. L., Hiroi, T., Liu, Y., & Taylor, L. A. (2011). The lunar rock and mineral characterization consortium: deconstruction and integrated mineralogical, petrologic, and spectroscopic analyses of mare basalts. *Meteoritics & Planetary Science*, 46, 228–251. <https://doi.org/10.1111/j.1945-5100.2010.01148.x>
- Isaacson, P. J., Petro, N. E., Pieters, C. M., Besse, S., Boardman, J. W., Clark, R. N., et al. (2013). Development, importance, and effect of a ground truth correction for the Moon Mineralogy Mapper reflectance data set. *Journal of Geophysical Research: Planets*, 118(3), 369–381. <https://doi.org/10.1002/jgre.20048>
- Ivanov, M. A., Hiesinger, H., van der Bogert, C. H., Orgel, C., Pasckert, J. H., & Head, J. W. (2018). Geologic history of the northern portion of the South Pole-Aitken Basin on the Moon. *Journal of Geophysical Research: Planets*, 123(10), 2585–2612. <https://doi.org/10.1029/2018JE005590>
- James, P. B., Smith, D. E., Byrne, P. K., Kendall, J. D., Melosh, H. J., & Zuber, M. T. (2019). Deep structure of the lunar South Pole–Aitken basin. *Geophysical Research Letters*. <https://doi.org/10.1029/2019GL082252>
- Jolliff, B. L., Gillis, J. J., Haskin, L. A., Korotev, R. L., & Wiczorek, M. A. (2000). Major lunar crustal terranes: Surface expressions and crust-mantle origins. *Journal of Geophysical Research*, 105(E2), 4197–4216. <https://doi.org/10.1029/1999JE001103>
- Jolliff, B. L., Watkins, R. C., Petro, N. E., Moriarty, D. P., Lawrence, S. J., Head, J. W., & Gaddis, L. R. (2017). Selecting and certifying landing sites for MoonRise in South Pole-Aitken Basin. *LPI*, 1964, 1326.
- Kadish, S. J., Fassett, C. I., Head, J. W., Smith, D. E., Zuber, M. T., Neumann, G. A., & Mazarico, E. (2011). A global catalog of large lunar crater (≥ 20 KM) from the Lunar Orbiter Laser Altimeter. In *Lunar and Planetary Science Conference* (XLII, abstract 1006).
- Khan, A., Connolly, J. A. D., Pommier, A., & Noir, J. (2014). Geophysical evidence for melt in the deep lunar interior and implications for lunar evolution. *Journal of Geophysical Research: Planets*, 119, 2197–2221. <https://doi.org/10.1002/2014JE004661>
- Klima, R. L., Dyar, M. D., & Pieters, C. M. (2011). Near-infrared spectra of clinopyroxenes: Effects of calcium content and crystal structure. *Meteoritics & Planetary Science*, 46(3), 379–395. <https://doi.org/10.1111/j.1945-5100.2010.01158.x>
- Klima, R. L., Pieters, C. M., & Dyar, M. D. (2007). Spectroscopy of synthetic Mg-Fe pyroxenes I: Spin-allowed and spin-forbidden crystal field bands in the visible and near-infrared. *Meteoritics & Planetary Science*, 42(2), 235–253. <https://doi.org/10.1111/j.1945-5100.2007.tb00230.x>
- Kuskov, O. L., Kronrod, V. A., & Kronrod, E. V. (2015). Thermochemical constraints on the thermal state, composition, and mineralogy of the upper mantle of the Moon: Evidence from the seismic models. *Solar System Research*, 49(2), 75–91. <https://doi.org/10.1016/j.pepi.2018.10.011>
- Lawrence, D. J., Elphic, R. C., Feldman, W. C., Gasnault, O., Genety, I., Maurice, S., & Prettyman, T. H. (2002). Small-area Thorium enhancements on the lunar surface. In *33rd Lunar and Planetary Science Conference* (Abstract #1970).
- Lawrence, D. J., Feldman, W. C., Barraclough, B. L., Binder, A. B., Elphic, R. C., Maurice, S., et al. (2000). Thorium abundances on the lunar surface. *Journal of Geophysical Research*, 105(E8), 20307–20331. <https://doi.org/10.1029/1999JE001177>
- Lawrence, D. J., Feldman, W. C., Elphic, R. C., Little, R. C., Prettyman, T. H., Maurice, S., & Binder, A. B. (2002). Iron abundances on the lunar surface as measured by the Lunar Prospector gamma-ray and neutron spectrometers. *Journal of Geophysical Research: Planets*, 107(E12), 13–21. <https://doi.org/10.1029/2001JE001530>
- Lawrence, D. J., Puetter, R. C., Elphic, R. C., Feldman, W. C., Hagerty, J. J., Prettyman, T. H., & Spudis, P. D. (2007). Global spatial deconvolution of Lunar Prospector Th abundances. *Geophysical Research Letters*, 34(3). <https://doi.org/10.1029/2006GL028530>
- Lemelin, M., Lucey, P. G., Miljković, K., Gaddis, L. R., Hare, T., & Ohtake, M. (2019). The compositions of the lunar crust and upper mantle: Spectral analysis of the inner rings of lunar impact basins. *Planetary and Space Science*, 165, 230–243. <https://doi.org/10.1016/j.pss.2018.10.003>

- Lemelin, M., Lucey, P. G., Song, E., & Taylor, G. J. (2015). Lunar central peak mineralogy and iron content using the Kaguya Multiband Imager: Reassessment of the compositional structure of the lunar crust. *Journal of Geophysical Research: Planets*, *120*(5), 869–887. <https://doi.org/10.1002/2014JE004778>
- Li, C., Liu, D., Liu, B., Ren, X., Liu, J., He, Z., et al. (2019). Chang'E-4 initial spectroscopic identification of lunar far-side mantle-derived materials. *Nature*, *569*(7756), 378–382. <https://doi.org/10.1038/s41586-019-1189-0>
- Lin, Y., Tronche, E. J., Steenstra, E. S., & van Westrenen, W. (2017). Evidence for an early wet Moon from experimental crystallization of the lunar magma ocean. *Nature Geoscience*, *10*(1), 14. <https://doi.org/10.1038/ngeo2845>
- Li, C., Su, Y., Pettinelli, E., Xing, S., Ding, C., Liu, J., et al. (2020). The Moon's farside shallow subsurface structure unveiled by Chang'E-4 Lunar Penetrating Radar. *Science advances*, *6*(9), eaay6898. <https://doi.org/10.1126/sciadv.aay6898>
- Li, H., Zhang, N., Liang, Y., Wu, B., Dygert, N. J., Huang, J., & Parmentier, E. M. (2019). Lunar cumulate mantle overturn: A model constrained by ilmenite rheology. *Journal of Geophysical Research: Planets*, *124*(5), 1357–1378. <https://doi.org/10.1029/2018JE005905>
- Loper, D. E., & Werner, C. L. (2002). On lunar asymmetries 1. Tilted convection and crustal asymmetry. *Journal of Geophysical Research*, *107*, E6. <https://doi.org/10.1029/2000JE001441>
- Lucey, P. G., Taylor, G. J., Hawke, B. R., & Spudis, P. D. (1998). FeO and TiO₂ concentrations in the South Pole-Aitken basin: Implications for mantle composition and basin formation. *Journal of Geophysical Research*, *103*(E2), 3701–3708. <https://doi.org/10.1029/97JE03146>
- Maurice, M., Tosi, N., Schwinger, S., Breuer, D., & Kleine, T. (2020). A long-lived magma ocean on a young Moon. *Science advances*, *6*(28), eaba8949. <https://doi.org/10.1126/sciadv.aba8949>
- Melosh, H. J. (1989). *Impact Cratering: A Geologic Process*, New York: Oxford University Press. <https://ui.adsabs.harvard.edu/abs/1989icgp.book.....M/abstract>
- Melosh, H. J., Kendall, J., Horgan, B., Johnson, B. C., Bowling, T., Lucey, P. G., & Taylor, G. J. (2017). South Pole–Aitken basin ejecta reveal the Moon's upper mantle. *Geology*, *45*(12), 1063–1066. <https://doi.org/10.1130/G39375.1>
- Miljkovic, K., Wieczorek, M. A., Collins, G. S., Solomon, S. C., Smith, D. E., & Zuber, M. T. (2015). Excavation of the lunar mantle by basin-forming impact events on the Moon. *Earth and Planetary Science Letters*, *409*, 243–251. <http://doi.org/10.1016/j.epsl.2014.10.041>
- Moriarty, D. P., III, & Pieters, C. M. (2016). Complexities in pyroxene compositions derived from absorption band centers: Examples from Apollo samples, HED meteorites, synthetic pure pyroxenes, and remote sensing data. *Meteoritics & Planetary Science*, *51*(2), 207–234. <http://doi.org/10.1111/maps.12588>
- Moriarty, D. P., & Petro, N. E. (2020). Mineralogical diversity of the Von Karman Region and the validity of mantle-derived olivine detections by Chang'E 4/Yutu-2. *Lunar and Planetary Science Conference*, (2326), 2660.
- Moriarty, D. P., & Pieters, C. M. (2015). The nature and origin of Mafic Mound in the South Pole-Aitken Basin. *Geophysical Research Letters*, *42*(19), 7907–7915. <http://doi.org/10.1002/2015GL065718>
- Moriarty, D. P., & Pieters, C. M. (2018). The character of South Pole-Aitken Basin: Patterns of surface and subsurface composition. *Journal of Geophysical Research: Planets*, *123*(3), 729–747. <http://doi.org/10.1002/2017JE005364>
- Moriarty, D. P., Pieters, C. M., & Isaacson, P. J. (2013). Compositional heterogeneity of central peaks within the South Pole-Aitken Basin. *Journal of Geophysical Research: Planets*, *118*(11), 2310–2322. <https://doi.org/10.1002/2013JE004376>
- Moriarty, D., Watkins, R., Valencia, S., Kendall, J., Evans, A., Dygert, N., & Petro, N. (2020). Evidence for a stratified Lunar Mantle preserved within the South Pole–Aitken Basin. *Mendeley Data*, *V1*. <https://doi.org/10.17632/rsb4p9wht9.1>
- Nakamura, R., Matsunaga, T., Ogawa, Y., Yamamoto, S., Hiroi, T., Saiki, K., et al. (2009). Ultramafic impact melt sheet beneath the South Pole–Aitken basin on the Moon. *Geophysical Research Letters*, *36*(22). <https://doi.org/10.1029/2009GL040765>
- National Research Council (2007). *The scientific context for exploration of the Moon*, Washington, DC: National Academies Press.
- Nelson, D. M., Koeber, S. D., Daud, K., Robinson, M. S., Watters, T. R., Banks, M. E., & Williams, N. R. (2014). Mapping lunar maria extents and lobate scarps using LROC image products. In *Lunar and Planetary Science Conference* (Vol. 45, March, pp. 2861).
- Oberbeck, V. R. (1975). The role of ballistic erosion and sedimentation in lunar stratigraphy. *Reviews of Geophysics*, *13*(2), 337–362. <https://doi.org/10.1029/RG013i002p00337>
- Ohtake, M., Uemoto, K., Yokota, Y., Morota, T., Yamamoto, S., Nakamura, R., et al. (2014). Geologic structure generated by large-impact basin formation observed at the South Pole-Aitken basin on the Moon. *Geophysical Research Letters*, *41*(8), 2738–2745. <https://doi.org/10.1002/2014GL059478>
- Parmentier, E. M., Zhong, S., & Zuber, M. T. (2002). Gravitational differentiation due to initial chemical stratification: origin of lunar asymmetry by the creep of dense KREEP?. *Earth and Planetary Science Letters*, *201*(3–4), 473–480. [https://doi.org/10.1016/S0012-821X\(02\)00726-4](https://doi.org/10.1016/S0012-821X(02)00726-4)
- Pasckert, J. H., Hiesinger, H., & van der Bogert, C. H. (2018). Lunar farside volcanism in and around the South Pole–Aitken basin. *Icarus*, *299*, 538–562. <https://doi.org/10.1016/j.icarus.2017.07.023>
- Pernet-Fisher, J. F., Deloule, E., & Joy, K. H. (2019). Evidence of chemical heterogeneity within lunar anorthosite parental magmas. *Geochimica et Cosmochimica Acta*, *266*, 109–130. <https://doi.org/10.1016/j.gca.2019.03.033>
- Petro, N. E., & Pieters, C. M. (2008). The lunar-wide effects of basin ejecta distribution on the early megaregolith. *Meteoritics & Planetary Science*, *43*(9), 1517–1529. <https://doi.org/10.1111/j.1945-5100.2008.tb01025.x>
- Pieters, C. M., Boardman, J., Buratti, B., Chatterjee, A., Clark, R., Glavich, T., et al. (2009). The Moon Mineralogy Mapper (M³) on Chandrayaan-1. *Current Science*, 500–505.
- Pieters, C. M., Head, J. W., Gaddis, L., Jolliff, B., & Duke, M. (2001). Rock types of South Pole-Aitken basin and extent of basaltic volcanism. *Journal of Geophysical Research*, *106*(E11), 28001–28022. <https://doi.org/10.1029/2000JE001414>
- Pieters, C. M., Taylor, L. A., Noble, S. K., Keller, L. P., Hapke, B., Morris, R. V., et al. (2000). Space weathering on airless bodies: Resolving a mystery with lunar samples. *Meteoritics & Planetary Science*, *35*(5), 1101–1107. <https://doi.org/10.1111/j.1945-5100.2000.tb01496.x>
- Potter, R. W., Collins, G. S., Kiefer, W. S., McGovern, P. J., & Kring, D. A. (2012). Constraining the size of the South Pole-Aitken basin impact. *Icarus*, *220*(2), 730–743. <https://doi.org/10.1016/j.icarus.2012.05.032>
- Prettyman, T. H., Feldman, W. C., Lawrence, D. J., McKinney, G. W., Binder, A. B., Elphic, R. C., et al. (2002). Library least squares analysis of lunar prospector gamma-ray spectra. *33rd Lunar and planetary science Conference* (Abstract #2012).
- Prettyman, T. H., Hagerty, J. J., Elphic, R. C., Feldman, W. C., Lawrence, D. J., McKinney, G. W., & Vaniman, D. T. (2006). Elemental composition of the lunar surface: Analysis of gamma ray spectroscopy data from Lunar Prospector. *Journal of Geophysical Research*, *111*, E12. <https://doi.org/10.1029/2005JE002656>
- Prissel, T. C., & Gross, J. (2020). On the petrogenesis of lunar troctolites: New insights into cumulate mantle overturn & mantle exposures in impact basins. *Earth and Planetary Science Letters*, *551*, 116531. <https://doi.org/10.1016/j.epsl.2020.116531>
- Purucker, M. E., Head, J. W., III, & Wilson, L. (2012). Magnetic signature of the lunar South Pole-Aitken basin: Character, origin, and age. *Journal of Geophysical Research*, *117*, E5. <https://doi.org/10.1029/2011JE003922>

- Qiao, L., Ling, Z., Fu, X., & Li, B. (2019). Geological characterization of the Chang'e-4 landing area on the lunar farside. *Icarus*, 333, 37–51. <https://doi.org/10.1016/j.icarus.2019.05.029>
- Rapp, J. F., & Draper, D. S. (2018). Fractional crystallization of the lunar magma ocean: Updating the dominant paradigm. *Meteoritics & Planetary Science*, 53(7), 1432–1455. <https://doi.org/10.1111/maps.13086>
- Ringwood, A. E., & Kesson, S. E. (1976). A dynamic model for mare basalt petrogenesis. In *Lunar and Planetary Science Conference Proceedings* (Vol. 7, April, pp. 1697–1722).
- Robbins, S. J. (2018). A new global database of lunar impact craters >1–2 km: 1. crater locations and sizes, comparisons with published databases, and global analysis. *Journal of Geophysical Research: Planets*, 3(0), 2018JE005592. <http://doi.org/10.1029/2018JE005592>
- Roberts, S. E., McCanta, M. C., Jean, M. M., & Taylor, L. A. (2019). New lunar meteorite NWA 10986: A mingled impact melt breccia from the highlands—A complete cross section of the lunar crust. *Meteoritics & Planetary Science*, 54(12), 3018–3035. <https://doi.org/10.1111/maps.13406>
- Ryunon, K. D., Moriarty, D. P., III, Denevi, B. W., Greenhagen, B. T., Morgan, G., Young, K. E., & Jozwiak, L. M. (2020). Impact melt facies in the moon's crism basin: Identifying, characterizing, and future radiogenic dating. *Journal of Geophysical Research: Planets*, 125(1) e2019JE006024. <https://doi.org/10.1029/2019JE006024>
- Sato, H., Robinson, M. S., Hapke, B., Denevi, B. W., & Boyd, A. K. (2014). Resolved Hapke parameter maps of the Moon. *Journal of Geophysical Research: Planets*, 119(8), 1775–1805. <https://doi.org/10.1002/2013JE004580>
- Sato, H., Robinson, M. S., Lawrence, S. J., Denevi, B. W., Hapke, B., Jolliff, B. L., & Hiesinger, H. (2017). Lunar mare TiO₂ abundances estimated from UV/Vis reflectance. *Icarus*, 296, 216–238. <https://doi.org/10.1016/j.icarus.2017.06.013>
- Shearer, C. K., Burger, P. V., Bell, A. S., Guan, Y., & Neal, C. R. (2015). Exploring the Moon's surface for remnants of the lunar mantle 1. Dunitic xenoliths in mare basalts. A crustal or mantle origin?. *Meteoritics & Planetary Science*, 50(8), 1449–1467. <https://doi.org/10.1111/maps.12480>
- Shearer, C. K., Elardo, S. M., Petro, N. E., Borg, L. E., & McCubbin, F. M. (2015). Origin of the lunar highlands Mg-suite: An integrated petrology, geochemistry, chronology, and remote sensing perspective. *American Mineralogist*, 100(1), 294–325. <https://doi.org/10.2138/am-2015-4817>
- Shearer, C. K., & Papike, J. J. (2005). Early crustal building processes on the moon: Models for the petrogenesis of the magnesian suite. *Geochimica et Cosmochimica Acta*, 69(13), 3445–3461. <https://doi.org/10.2138/am-2015-4817>
- Smith, D. E., Zuber, M. T., Neumann, G. A., Lemoine, F. G., Mazarico, E., Torrence, M. H., et al. (2010). Initial observations from the lunar orbiter laser altimeter (LOLA). *Geophysical Research Letters*, 37, 18. <https://doi.org/10.1029/2010GL043751>
- Snyder, G. A., Taylor, L. A., & Neal, C. R. (1992). A chemical model for generating the sources of mare basalts: Combined equilibrium and fractional crystallization of the lunar magmasphere. *Geochimica et Cosmochimica Acta*, 56(10), 3809–3823. [https://doi.org/10.1016/0016-7037\(92\)90172-F](https://doi.org/10.1016/0016-7037(92)90172-F)
- Speyerer, E. J., Robinson, M. S., & Denevi, B. W., & LROC Team (2011). Lunar Reconnaissance Orbiter Camera Morphological Map of the Moon. In *Lunar and Planetary Science Conference* (Vol. 42, 2387).
- Speyerer, E. J., Wagner, R. V., Robinson, M. S., Licht, A., Thomas, P. C., Becker, K., et al. (2016). Pre-flight and on-orbit geometric calibration of the Lunar Reconnaissance Orbiter Camera. *Space Science Reviews*, 200(1–4), 357–392. <https://doi.org/10.1007/s11214-014-0073-3>
- Spudis, P. D., & Davis, P. A. (1986). A chemical and petrological model of the lunar crust and implications for lunar crustal origin. *Journal of Geophysical Research*, 91(B13), E84–E90. <https://doi.org/10.1029/JB091B13p00E84>
- Spudis, P. D., Martin, D. J., & Kramer, G. (2014). Geology and composition of the Orientale Basin impact melt sheet. *Journal of Geophysical Research: Planets*, 119(1), 19–29. <https://doi.org/10.1002/2013JE004521>
- Steenstra, E. S., Berndt, J., Klemme, S., Fei, Y., & van Westrenen, W. (2020). A possible high-temperature origin of the Moon and its geochemical consequences. *Earth and Planetary Science Letters*, 538, 116222. <https://doi.org/10.1016/j.epsl.2020.116222>
- Stöffler, D., Knöll, H. D., Marvin, U. B., Simonds, C. H., & Warren, P. H. (1980). Recommended classification and nomenclature of lunar highland rocks—a committee report. *Conference on the Lunar Highlands Crust, Houston, Tex., November 14–16, 1979, Proceedings*. (A81-26201 10-91) New York and Oxford: Pergamon Press, pp. 51–70.
- Stuart-Alexander, D. E. (1978). *Geologic map of the central far side of the Moon*, 1047, Denver, CO: USGS.
- Sun, Y., Li, L., & Zhang, Y. (2017). Detection of Mg-spinel bearing central peaks using M3 images: Implications for the petrogenesis of Mg-spinel. *Earth and Planetary Science Letters*, 465, 48–58. <https://doi.org/10.1016/j.epsl.2017.01.019>
- Sunshine, J. M., Pieters, C. M., & Pratt, S. F. (1990). Deconvolution of mineral absorption bands: An improved approach. *Journal of Geophysical Research*, 95(B5), 6955–6966. <https://doi.org/10.1029/JB095iB05p06955>
- Tartèse, R., Anand, M., Gattacceca, J., Joy, K. H., Mortimer, J. I., Pernet-Fisher, J. F., et al. (2019). Constraining the evolutionary history of the moon and the inner solar system: A case for new returned lunar samples. *Space Science Reviews*, 215(8), 54. <https://doi.org/10.1007/s11214-019-0622-x>
- Taylor, G. J., & Wieczorek, M. A. (2014). Lunar bulk chemical composition: a post-Gravity Recovery and Interior Laboratory reassessment. *Philosophical Transactions of the Royal Society A: Mathematical, Physical and Engineering Sciences*, 372(2024), 20130242. <http://doi.org/10.1098/rsta.2013.0242>
- Thiemens, M. M., Spring, P., et al. (2019). Early Moon formation inferred from hafnium-tungsten systematics. *Nature Geoscience*. <https://doi.org/10.1038/s41561-019-0398-3>
- Tompkins, S., & Pieters, C. M. (1999). Mineralogy of the lunar crust: Results from Clementine. *Meteoritics & Planetary Science*, 34(1), 25–41. <https://doi.org/10.1111/j.1945-5100.1999.tb01729.x>
- Trowbridge, A. J., Johnson, B. C., Freed, A. M., & Melosh, H. J. (2020). Why the lunar South Pole-Aitken Basin is not a mascon. *Icarus*, 352, 113995. <https://doi.org/10.1016/j.icarus.2020.113995>
- Tsunakawa, H., Shibuya, H., Takahashi, F., Shimizu, H., Matsuhashi, M., Matsuoka, A., & Iijima, Y. (2010). Lunar magnetic field observation and initial global mapping of lunar magnetic anomalies by MAP-LMAG onboard SELENE (Kaguya). *Space Science Reviews*, 154(1–4), 219–251. <https://doi.org/10.1007/s11214-010-9652-0>
- Uemoto, K., Ohtake, M., Haruyama, J., Matsunaga, T., Yamamoto, S., Nakamura, R., et al. (2017). Evidence of impact melt sheet differentiation of the lunar South Pole-Aitken basin. *Journal of Geophysical Research: Planets*, 122(8), 1672–1686. <https://doi.org/10.1002/2016JE005209>
- van Orman, J. A., & Grove, T. L. (2000). Origin of lunar high-titanium ultramafic glasses: Constraints from phase relations and dissolution kinetics of clinopyroxene-ilmenite cumulates. *Meteoritics & Planetary Science*, 35(4), 783–794. <https://doi.org/10.1111/j.1945-5100.2000.tb01462.x>
- Vaughan, W. M., & Head, J. W. (2014). Impact melt differentiation in the South Pole-Aitken basin: Some observations and speculations. *Planetary and Space Science*, 91, 101–106. <https://doi.org/10.1016/j.pss.2013.11.010>

- Wagner, R. V., Speyerer, E. J., & Robinson, M. S., & LROC Team (2015). New mosaicked data products from the LROC team. In *Lunar and Planetary Science Conference* (Vol. 46 abstract #1473).
- Warren, P. H., & Wasson, J. T. (1978). Urkrep: The Last Dregs of the Lunar Magma Ocean. In *Lunar and Planetary Science Conference* (Vol. 9, March, 1231–1233).
- Warren, P. H., & Wasson, J. T. (1979). The origin of KREEP. *Reviews of Geophysics*, 17(1), 73–88. <https://doi.org/10.1029/RG017i001p00073>
- Wasson, J. T., & Warren, P. H. (1980). Contribution of the mantle to the lunar asymmetry. *Icarus*, 44(3), 752–771. [https://doi.org/10.1016/0019-1035\(80\)90142-6](https://doi.org/10.1016/0019-1035(80)90142-6)
- Weber, R. C., Lin, P. Y., Garnero, E. J., Williams, Q., & Lognonne, P. (2011). Seismic detection of the lunar core. *Science*, 331(6015), 309–312. <https://doi.org/10.1126/science.1199375>
- Whitaker, E. A. (1981). *The lunar Procellarum basin, Multi-ring basins: Formation and evolution; Proceedings of the Lunar and Planetary Science Conference A82-39033*, 19–91, 105–111. New York: Pergamon Press.
- Whitten, J. L., & Head, J. W. (2015). Lunar cryptomaria: Physical characteristics, distribution, and implications for ancient volcanism. *Icarus*, 247, 150–171. <https://doi.org/10.1016/j.icarus.2014.09.031>
- Wieczorek, M. A., Phillips, R. J. (1998). Potential anomalies on a sphere: Applications to the thickness of the lunar crust. *Journal of Geophysical Research: Planets*, 103(E1), 1715–1724. <http://doi.org/10.1029/97je03136>
- Wieczorek, M. A., Neumann, G. A., Nimmo, F., Kiefer, W. S., Taylor, G. J., Melosh, H. J., et al. (2013). The crust of the Moon as seen by GRAIL. *Science*, 339(6120), 671–675. <https://doi.org/10.1126/science.1231530>
- Wieczorek, M. A., Weiss, B. P., & Stewart, S. T. (2012). An impactor origin for lunar magnetic anomalies. *Science*, 335(6073), 1212–1215. <https://doi.org/10.1126/science.1214773>
- Wieczorek, M. A., & Zuber, M. T. (2001a). A Serenitatis origin for the Imbrian grooves and South Pole-Aitken thorium anomaly. *Journal of Geophysical Research*, 106(E11), 27853–27864. <https://doi.org/10.1029/2000JE001384>
- Wieczorek, M. A., & Zuber, M. T. (2001b). The composition and origin of the lunar crust: Constraints from central peaks and crustal thickness modeling. *Geophysical Research Letters*, 28(21), 4023–4026. <https://doi.org/10.1029/2001GL012918>
- Wilhelms, D. E., John, F., & Trask, N. J. (1987). In McCauley, & N. J. Trask (Eds.), *The geologic history of the Moon*, Professional Paper (1348 ed., pp. 1–302). Denver, CO: USGS. <https://doi.org/10.3133/pp1348>
- Wood, J. A., Dickey, J. S., Jr, Marvin, U. B., & Powell, B. N. (1970). Lunar anorthosites and a geophysical model of the moon. *Geochimica et Cosmochimica Acta Supplement*, 1, 965.
- Yamamoto, S., Nakamura, R., Matsunaga, T., Ogawa, Y., Ishihara, Y., Morota, T., et al. (2010). Possible mantle origin of olivine around lunar impact basins detected by SELENE. *Nature Geoscience*, 3(8), 533. <https://doi.org/10.1038/ngeo897>
- Yamamoto, S., Nakamura, R., Matsunaga, T., Ogawa, Y., Ishihara, Y., Morota, T., et al. (2012). Olivine-rich exposures in the South Pole-Aitken basin. *Icarus*, 218(1), 331–344. <https://doi.org/10.1016/j.icarus.2011.12.012>
- Yingst, R. A., & Head, J. W., III (1999). Geology of mare deposits in South Pole-Aitken basin as seen by Clementine UV/VIS data. *Journal of Geophysical Research*, 104(E8), 18957–18979. <https://doi.org/10.1029/1999JE900016>
- Yu, S., Tosi, N., Schwinger, S., Maurice, M., Breuer, D., & Xiao, L. (2019). Overturn of Ilmenite-Bearing Cumulates in a Rheologically Weak Lunar Mantle. *Journal of Geophysical Research: Planets*, 124(2), 418–436. <https://doi.org/10.1029/2018JE005739>
- Zhang, N., Dygert, N., Liang, Y., & Parmentier, E. M. (2017). The effect of ilmenite viscosity on the dynamics and evolution of an overturned lunar cumulate mantle. *Geophysical Research Letters*, 44(13), 6543–6552. <https://doi.org/10.1002/2017GL073702>
- Zhang, J., Zhou, B., Lin, Y., Zhu, M. H., Song, H., Dong, Z., et al. (2020). Lunar regolith and substructure at Chang'E-4 landing site in South Pole-Aitken basin. *Nature Astronomy*, 1–6. <https://doi.org/10.1038/s41550-020-1197-x>
- Zhao, Y., de Vries, J., van den Berg, A. P., Jacobs, M. H. G., & van Westrenen, W. (2019). The participation of ilmenite-bearing cumulates in lunar mantle overturn. *Earth and Planetary Science Letters*, 511, 1–11. <https://doi.org/10.1016/j.epsl.2019.01.022>